Available online at www.sciencedirect.com
ScienceDirect
Geochimica et Cosmochimica Acta 73 (2009) 1924–1944
Geochimica et Cosmochimica Acta
www.elsevier.com/locate/gca

An integrated sulfur isotope model for Namibian shelf sediments

Andrew W. Dale [a,*], Volker Brüchert [b], Marc Alperin [c], Pierre Regnier [a,d]

[a] Department of Earth Sciences – Geochemistry, Utrecht University, The Netherlands
[b] Department of Geology and Geochemistry, Stockholm University, Stockholm, Sweden
[c] Department of Marine Sciences, University of North Carolina, Chapel Hill, USA
[d] Department of Earth and Environmental Sciences, CP 160/02, Université Libre de Bruxelles, 50 Av. F. D. Roosevelt, B-1050 Brussels, Belgium

Received 8 November 2007; accepted in revised form 7 December 2008; available online 25 December 2008

Abstract

In this study the sulfur cycle in the organic-rich mud belt underlying the highly productive upwelling waters of the Namibian shelf is quantified using a 1D reaction-transport model. The model calculates vertical concentration and reaction rate profiles in the top 500 cm of sediment which are compared to a comprehensive dataset which includes carbon, sulfur, nitrogen and iron compounds as well as sulfate reduction (SR) rates and stable sulfur isotopes (^{32}S, ^{34}S). The sulfur dynamics in the well-mixed surface sediments are strongly influenced by the activity of the large sulfur bacteria *Thiomargarita namibiensis* which oxidize sulfide (H_2S) to sulfate (SO_4^{2-}) using sea water nitrate (NO_3^-) as the terminal electron acceptor. Microbial sulfide oxidation (SOx) is highly efficient, and the model predicts intense cycling between SO_4^{2-} and H_2S driven by coupled SR and SOx at rates exceeding 6.0 mol S m^{-2} y^{-1}. More than 96% of the SR is supported by SOx, and only 2–3% of the SO_4^{2-} pool diffuses directly into the sediment from the sea water. A fraction of the SO_4^{2-} produced by *Thiomargarita* is drawn down deeper into the sediment where it is used to oxidize methane anaerobically, thus preventing high methane concentrations close to the sediment surface. Only a small fraction of total H_2S production is trapped as sedimentary sulfide, mainly pyrite (FeS_2) and organic sulfur (S_{org}) (~0.3 wt.%), with a sulfur burial efficiency which is amongst the lowest values reported for marine sediments (<1%). Yet, despite intense SR, FeS_2 and S_{org} show an isotope composition of ~5 ‰ at 500 cm depth. These heavy values were simulated by assuming that a fraction of the solid phase sulfur exchanges isotopes with the dissolved sulfide pool. An enrichment in H_2S of ^{34}S towards the sediment-water interface suggests that *Thiomargarita* preferentially remove $H_2{}^{32}S$ from the pore water. A fractionation of 20–30‰ was estimated for SOx (ε_{SOx}) with the model, along with a maximum fractionation for SR (ε_{SR-max}) of 100‰. These values are far higher than previous laboratory-based estimates for these processes. Mass balance calculations indicate negligible disproportionation of autochthonous elemental sulfur; an explanation routinely cited in the literature to account for the large fractionations in SR. Instead, the model indicates that repeated multi-stepped sulfide oxidation and intracellular disproportionation by *Thiomargarita* could, in principle, allow the measured isotope data to be simulated using much lower fractionations for ε_{SOx} (5‰) and ε_{SR} (78‰).

1. INTRODUCTION

The Namibian shelf (southwest Africa) is located within the Benguela upwelling system and is characterized by near-perennial upwelling of South Atlantic Central Water (SACW) and Eastern SACW, high productivity and bottom water anoxia (Bailey et al., 1985; Chapman and Shannon, 1985). The water depth on the inner shelf is quite shallow (~100 m), which allows a significant amount of fresh phytodetritus to be deposited at the sediment-water interface. The absence of dissolved oxygen in the bottom water enhances the accumulation of particulate organic carbon (POC) in the sea floor, which reaches up to 15% dry weight (Inthorn et al., 2006). Free methane gas has been detected

* Corresponding author. Present address: Leibniz-Institut für Meereswissenschaften, IFM-GEOMER, Wischhofstr. 1-3, D-24148 Kiel, Germany. Fax: +31 30 253 5302.
E-mail address: dale@geo.uu.nl (A.W. Dale).

0016-7037/$ - see front matter © 2008 Elsevier Ltd. All rights reserved.
doi:10.1016/j.gca.2008.12.015

deep in the mud wherever the sediment thickness surpasses 4 m (Emeis et al., 2004).

The above factors contribute to a sediment geochemistry which is markedly different from that of typical continental shelf sediments. The deposition of extremely labile phytoplankton-derived organic matter generates rates of bacterial sulfate reduction (SR) from the sediment-water interface down to 10–15 cm depth which are markedly high for passive margin sediments (100 mM y^{-1} of SO_4^{2-}) (Brüchert et al., 2003). SR produces copious quantities of dissolved sulfide (H_2S) which can accumulate to 10 mM or more in the surface layers. The chemical oxidants for H_2S commonly found in shelf sediments are either absent (O_2) or present at very low concentrations (Fe(III), Mn(IV); Borchers et al. (2005)). The pronounced boundaries between the oxic, suboxic and anoxic sediments, within which redox transformations of sulfur coupled to Fe, Mn and O_2 cycling normally occurs (Canfield et al., 2005), are therefore not present here. Consequently, the subsurface H_2S can be released episodically to the water column, producing ephemeral periods of euxinia during which seawater H_2S concentrations increase to 0.1 mM (Brüchert et al., 2006). Extreme, yet rare, H_2S emissions from the sediment can have severe impacts on local fisheries (Bailey et al., 1985).

The redox dynamics in the Namibian shelf is thus highly specific. In addition, the H_2S flux towards the sediment-water interface is mostly consumed by the non-phototrophic large sulfur bacteria *Thiomargarita namibiensis* (Schulz et al., 1999; Brüchert et al., 2003). *Thiomargarita namibiensis* catalyzes the reaction between H_2S and nitrate (NO_3^-) to produce sulfate (SO_4^{2-}) and ammonium (NH_4^+), similar to filamentous *Beggiatoa* and *Thioploca* species (Fossing et al., 1995; Ferdelman et al., 1997; Otte et al., 1999; Preisler et al., 2007). These bacteria tend to colonize areas on the Namibian shelf characterized by occasional euxinia and high subsurface SR rates (Brüchert et al., 2003). *Beggiatoa*, *Thiomargarita* and *Thioploca* are vacuolated and can store large amounts of NO_3^- at concentrations up to 800 mM (Schulz et al., 1999). However, in contrast to *Thioploca* and *Beggiatoa*, *Thiomargarita* are non-filamentous and believed to be non-motile, such that externally-driven sediment resuspension has been proposed as the mechanism which allows these bacteria to access the seawater and regenerate their internal NO_3^- reservoir (Schulz and Jørgensen, 2001). More recently, *Thiomargarita* have been detected in hydrocarbon seep sediments in the Gulf of Mexico (Kalanetra et al., 2005).

Very little quantitative information is known about the interactions between *Thiomargarita* and their geochemical surroundings. This knowledge gap provides the impetus for this study, that is, to quantify the dynamic interplay of the nitrogen, sulfur and carbon cycles at a representative site where *Thiomargarita* have been detected. The data presented, which include the NO_3^- content of *Thiomargarita* as well as pore water and solid phase stable sulfur isotopes (^{32}S, ^{34}S), are primarily used to confirm the results of a steady-state reaction-transport model (RTM). The factors contributing to the isotope distributions in the sediment are constrained by explicitly modeling the individual sulfur isotopes of the major dissolved and solid compounds, including the pyrite and organic sulfur sinks (Brüchert et al., 2000). Relatively few RTMs of marine sediments have incorporated sulfur isotopes (e.g. Goldhaber and Kaplan, 1980; Rudnicki et al., 2001; Wortmann et al., 2001) even though the relevant theory was developed three decades ago (Jørgensen, 1979). Because RTMs can account for differential diffusion of isotopes, a common goal of these modeling studies has been to determine the fractionation factor (α) for dissimilatory SR. For reasons which are still unclear, the fractionations, $\varepsilon(= 1000 \times (\alpha - 1)$, derived using RTMs (60–77‰ in the above studies) are more comparable to the theoretical equilibrium isotope fractionations (~70–80‰, Farquhar et al., 2003) than to the values measured under laboratory conditions (2–47‰). Fractionation of sulfide during sulfide oxidation (SOx) by *Thiomargarita, Thioploca* or *Beggiatoa* has not been measured because these bacteria have not yet been isolated and maintained in pure culture. Experimental evidence suggests, however, that microbially-mediated SOx is associated with a small normal (i.e. preferential dissimilation of the lighter isotope) fractionation ($\varepsilon \approx 5$‰) (Fry et al., 1985, 1988). Therefore, in addition to gaining an insight into the coupled C, N and S cycles which cannot be achieved from visual interpretation of the data alone, the present study provides also an estimation of the fractionation during SR in Namibian shelf sediments as well as a first estimation of sulfide fractionation during oxidation by *Thiomargarita* at this site.

2. MATERIAL AND ANALYTICAL METHODS

2.1. Study area and oceanographic setting

The Namibian shelf lies in the eastern boundary current system of the Southeast Atlantic where offshore trade winds engender upwelling of South Atlantic Central Water (SACW) and Eastern SACW along the coast (Bailey et al., 1985; Chapman and Shannon, 1985; Mohrholz et al., 2008). The bottom sediments lying parallel to the shelf between 20.6 and 25.5°S (average water depth ~100 m) enclose ~25,000 km^2 of an organic-rich mud belt, with an average thickness of 5 m and surpassing 15 m over topographical depressions (Bremner, 1980). Sediment cores were retrieved from Station 226680 (23°46.52′S, 014°17.96′E, 110 m water depth,) during RV Meteor cruise M48-2 on 9th August 2000 (Emeis et al., 2002). The sampling site is located within the mud belt, defined by Monteiro et al. (2005) as the mid-shelf area (~20–24°S) where water depths are between 50 and 140 m. Inthorn et al. (2006) reported that lateral (offshore) sediment transport in nepheloid layers is an important mechanism for organic carbon transport down the continental slope of the Benguela upwelling system. Towards the coast, lateral transport is restricted, and organic matter input mainly occurs vertically through deposition of fresh organic matter (Inthorn et al., 2006). During summer, the hypoxic SACW lies over the shelf and, in conjunction with high primary productivity (average 217 mmol C m^{-2} d^{-1}; Brüchert et al., 2006), the bottom waters become anoxic. Chlorophyll *a* concentration in the surface water may be as high as 30 mg m^{-3} (Barlow, 1982). At the time of sampling, the bottom water oxygen

concentration was <3 μM and hydrogen sulfide was below detection limit (Emeis et al., 2002).

2.2. Sedimentology and stratigraphy

The surface sediments at site 226680 and throughout the mud belt are diatomaceous oozes with low carbonate and terrigenous fractions (Borchers et al., 2005). They are extremely rich in labile POC with concentrations in excess of 15% dry weight (Inthorn et al., 2006). Macrofauna were absent in the topmost centimeters of the sediment core, yet some detritus of gastropods, bivalve shells, and fish scales were present. Based on the analysis of a gravity core (226670 SL-6) collected at the same location, the sediment consisted of silty clay to clayey silt, with both laminated and homogeneous intervals of dark olive gray to light greenish olive color (Emeis et al., 2002). The surface sediments in the upper 12 cm were unlaminated and very soft and soupy, with a wet density of 1.1 g cm^{-3}. Below this layer, laminations became prominent to 120 cm depth, and then the sediment was homogeneous and compact down to 142 cm. With increasing depth the sediment became less compact and laminations reappeared, being particularly prominent from 190 to 205 cm. The individual laminae were greenish and olive in color with a thickness of 1–3 mm. The color of laminations from 236 to 336 cm varied between light and dark. Observations of shell debris became more frequent below 215 cm depth. Intact bivalve shells were found at 55 and 68 cm depth.

2.3. Sampling

Bottom water data on temperature, O_2 and NO_3^- concentrations were acquired with a SBE 911+ CTD equipped with an oxygen optode sensor mounted with a rosette sampler in a plastic-covered stainless steel frame. The lowermost cast was generally 1 m above the sediment. An Oktopus multicorer was used to obtain undisturbed near-surface sediment down to 48 cm depth and a gravity corer was used to collect a long sediment core of 472 cm length. Part of the surface sediment was lost during gravity coring and the geochemical concentration profiles measured in the two sediment cores were superimposed to account for the loss of sediment (~10 cm). The data in this study are plotted using this corrected composite depth. Sediment from the multicore tubes was subsampled in a nitrogen-filled glove bag in 1-cm intervals to a depth of 5 cm, and then in 2-cm intervals to the bottom of the core. The sediment sections were immediately placed into a Reeburgh-type pneumatic pore water squeezer using nitrogen gas. About 20 ml of the extracted pore water was filtered through a 0.2 μm cellulose-nitrate filter and preserved with 5 ml of 5% zinc acetate solution to precipitate dissolved sulfide as zinc sulfide (ZnS). The squeezed sediment was stored frozen at −20 °C until further analysis. The gravity core was cut into 1 m sections which were capped at each end. The sections were extruded with a piston in a nitrogen-filled glove box and sub-sampled with cut-off 50 ml syringes. The pore water was squeezed sediment were treated as described above until further analysis. For dissolved methane, duplicate cut-off syringes with a volume of 3 cm^3 were inserted into the sediment in the same depth intervals and the contents were transferred to serum vials containing 5 ml of 2.5% NaOH solution.

2.4. Porosity and sediment accumulation rates

The sediment density was determined from the weight and volume of the dry sediment. Porosity was determined from the dry sediment weight and water content without salt correction after drying the samples at 80 °C for 48 h. Sediment accumulation rates were determined from ^{210}Pb-activities using γ-spectroscopy of freeze-dried ground sediment (Emeis et al., 2007).

2.5. Pore water chemical analyses

Dissolved sulfide was analyzed spectrophotometrically on board following the method of Cline (1969) after appropriate dilution with double de-ionized water. Unless otherwise stated, hydrogen sulfide in this article refers to the sum of dissolved sulfide species and is reported as H_2S. Dissolved sulfate (SO_4^{2-}) was determined by ion chromatography following the methods described in Brüchert et al. (2003). Dissolved methane was analyzed from the headspace of sediment slurries in the serum vials. Fifty microliter from the headspace were injected into a HP 5890 gas chromatograph equipped with an FID and a Poropak column following methods described in Fossing et al. (2000).

2.6. Intracellular nitrate concentration in Thiomargarita

Intracellular NO_3^- concentrations of *Thiomargarita* cells were determined by sectioning one 26 mm diameter sediment core into 1 cm sections down to a depth of 10 cm. To avoid cell rupture, this core was not squeezed as described above. NO_3^- concentrations were determined from cells of *Thiomargarita* picked from 0.5 ml of sediment with a pasteur pipette. The cells were washed repeatedly with double de-ionized water (DDIW), and then transferred to 250 μl of DDIW. Subsequent repeated freezing and thawing aided cell rupture and NO_3^- release. The NO_3^- concentration was then determined by chemoluminescence using an $NO–NO_2–NO_x$ analyzer (Braman and Hendricks, 1989). Measured intracellular NO_3^- concentrations are reported here as molar concentration units in pore water using the average biovolume of *Thiomargarita* measured on 50–100 cells, the number of cells per ml sediment and the porosity.

2.7. Solid phase analyses

The sediment was freeze-dried, and approximately 5 mg were weighed into zinc capsules and analyzed for total carbon, nitrogen, and sulfur concentrations on a Carlo Erba NA 1500 elemental analyzer. A second batch of sediment was weighed into silver cups before adding 3–5 drops of 1 N HCl to remove any calcium carbonate. The cups were then oven-dried overnight and analyzed for their residual carbon concentration, interpreted as organic carbon. Inorganic carbon was subsequently determined by difference.

Reactive iron minerals were extracted from 100–300 mg of frozen sediment for 1.5 h with sodium dithionite (0.5 g/10 ml) buffered with 0.35 M acetate/0.2 M sodium citrate to a pH of 4.8 (Kostka and Luther, 1994). The extract was centrifuged and filtered. Total dissolved iron (50 µl sample per 2 ml) was derivatized with a ferrozine solution (1 g ferrozine per liter containing 12 g HEPES adjusted to pH 7). Twenty milliliter of hydroxylamine hydrochloride (10 g/100 ml) were added as a reducing agent. The solutions were analyzed with a spectrophotometer at 562 nm (Stookey, 1970).

Between 2 and 8 g of dried sediment was mixed three times in an ultrasonic bath with 50 ml of methanol, and the extracts were pooled and stored for elemental sulfur analysis by HPLC. The residual sediment was placed in a nitrogen-flushed flask, and after 15 min, 20 ml of 6 N HCl were added to the flask to extract acid-volatile sulfide (AVS) including easily reducible sulfides such as greigite. Evolved hydrogen sulfide was flushed from the flask and trapped in 10 ml of 0.1 N $AgNO_3$. The extraction continued until Ag_2S precipitation in the trap ceased (~1 h). Subsequently, 12 ml of 1 M $CrCl_2$ solution were added and the solution was boiled for an hour to extract chromium-reducible sulfide (CRS). $CrCl_2$ was prepared from $CrCl_3$ by reduction with elemental zinc pre-cleaned in 6 N HCl for 1 h. CRS was trapped as described above. Ag_2S precipitates from the AVS and CRS distillations were filtered, washed, and dried. AVS and CRS concentrations were determined gravimetrically. For mass balance calculations, AVS and CRS were assumed to be equivalent to iron monosulfide (FeS) and pyrite (FeS_2), respectively.

2.8. Stable sulfur isotopes

The frozen pore waters were thawed and filtered through 0.2 µm cellulose nitrate filters in the laboratory. The filter with the ZnS precipitate was carefully placed into a solution containing 0.1 N $AgNO_3$ and left overnight. The following day, the filter with Ag_2S was carefully removed from the solution and dried. The Ag_2S was scraped from the filter and between 100 and 400 µg were weighed into tin capsules together with a fivefold excess of V_2O_5. The filtered aliquot of the pore water was placed in a beaker and acidified to pH 3 using 1 N HCl and heated. Fifteen milliliter of 1 M $BaCl_2$ solution was added to the beaker. After 2 h the heated solution was cooled and the $BaSO_4$ precipitate was filtered through 0.2 µm cellulose–nitrate filters. The stable sulfur isotope composition was analyzed on a ThermoFinnigan Delta Plus isotope ratio mass spectrometer coupled via a Conflo II to a Eurovector CNS elemental analyzer. Isotope values are reported in the standard delta notation relative to Canyon Diablo Triolite (CDT = 0.0450045). Replicate measurements of the IAEAS2 Ag_2S standards agreed within ±0.4‰ for runs in the signal range between 0.4 and 5.1 V on mass 64.

2.9. Sulfate reduction rates

^{35}S-sulfate reduction (SR) rates were determined with the whole core incubation method of Jørgensen (1978) following the procedures described in Brüchert et al. (2003). Two sub-cores (26 mm) per station were injected at 1 cm intervals through silicon-sealed holes with 2 µl $^{35}SO_4^{2-}$ tracer (80 kBq ml^{-1}). Cores were incubated for 4 h in the dark at bottom water temperature. The core was sliced in 1 cm segments and the sections mixed with 20 ml of 20% zinc acetate solution and frozen. Bacterial SR rates were quantified by the one-step acidic chromium reduction method (Fossing and Jørgensen, 1989). Total reduced inorganic sulfur TRI^{35}S ($Fe^{35}S$, ^{35}S, $Fe^{35}S_2$, $Zn^{35}S$) from the reduction of $^{35}SO_4^{2-}$ was distilled off and the liberated $H_2{}^{35}S$ trapped in 10 ml zinc acetate. $^{35}SO_4^{2-}$ was separated from the sediment and the reduced sulfur compounds by centrifugation. TRI^{35}S and $^{35}SO_4^{2-}$ were counted on a Canberra-Packard 2400 TR liquid scintillation counter (Packard Ultima Gold XR scintillation fluid). Details of the method, blank correction, and the calculation of SR rates are described in Ferdelman et al. (1999).

All analytical data presented in this paper are supplied in the electronic annex.

3. MODEL SET-UP

3.1. Material transport and boundary conditions

The model describes the dynamics of 10 solutes and 16 solids (Table 1). The one-dimensional mass-conservation equation (Berner, 1980; Boudreau, 1997; Berg et al., 2003) resolves the depth concentration profiles of solids and solutes (C) along the vertical x axis with time:

$$(\xi\varphi + \rho_s(1-\varphi)\kappa)\frac{\partial C}{\partial t} = \frac{\partial}{\partial x}\left((\xi\varphi(D_S + D_M) + \rho_s(1-\varphi)D_M\kappa)\frac{\partial C}{\partial x}\right) - \frac{\partial}{\partial x}((\zeta[\varphi v] + \rho_s[(1-\varphi)v]\kappa)C) + \zeta\varphi\Phi(C_0 - C) + \sum r \quad (1)$$

Table 1
Model boundary conditions at the sediment-water interface. Solutes and solids are defined as fixed concentrations and fluxes, respectively.

Solutes	µM	Solids	µmol cm^{-2} y^{-1}
$^{32}SO_4^{2-}$	27,150	G_1	700
$^{34}SO_4^{2-}$	1246	G_2	450
$H_2{}^{32}S$	5.737	G_3	160
$H_2{}^{34}S$	0.262	$Fe(OH)_{3\text{-}A}$	9.0
CH_4	1.0×10^{-6}	$Fe(OH)_{3\text{-}B}$	0.1
NO_3^-	800[†]	$^{32}S^0$	0.0
Fe^{2+}	0.0	$^{34}S^0$	0.0
NH_4^+	1.0	≡NH_4-ads	0.0
H_2	1.0×10^{-4}	≡Fe-ads	0.0
ΣCO_2	2000	$Fe^{32}S$	0.0
		$Fe^{34}S$	0.0
		$Fe^{32}S_2$	0.0
		$Fe^{34}S_2$	0.0
		$Fe^{32,34}S_2$	0.0
		$^{32}S_{org}$	0.0
		$^{34}S_{org}$	0.0

[†] Pore water normalized concentration.

with $\zeta = 1, \kappa = 0$ if C is a solute
$\zeta = 0, \kappa = 1$ if C is a solid
$\zeta = 1, \kappa = K$ if C is a solute which adsorbs onto particles

In Eq. (1), t is time, ρ_s is the dry sediment density, φ is the depth-dependent porosity, C_0 is the solute concentration at the top of the core, D_S is the in situ molecular diffusion coefficient, D_M is an additional depth-variable mixing term (see below), v is the sediment burial velocity, Φ describes the non-local transport of NO_3^- (see below), K is the apparent adsorption coefficient (for ferrous iron, Fe^{2+}, and ammonium, NH_4^+), and Σr is the sum of production and consumption rates due to biogeochemical reactions. The numerical solution of the coupled partial differential equations was computed with the Biogeochemical Reaction Network Simulator (BRNS) (Aguilera et al., 2005) until steady-state was reached (i.e. no temporal change in concentration or rate at a given depth). Table 2 provides values for the physical parameters and variables used in the model.

The measured porosity data show a rapid initial decrease down to ~15 cm followed by a more attenuated decrease below this depth to the base of the core (Fig. 1a). This behavior was described in the model using a double-exponential formula assuming steady-state sediment compaction:

$$\varphi = \varphi_0[(1-p)\ \exp(-x/x_{por1}) + p\ \exp(-x/x_{por2})] \quad (2)$$

where φ_0 is the porosity at the sediment-water interface, p is the partitioning coefficient between the two exponential functions, and x_{por1} and x_{por2} are the depth attenuation lengths of porosity. The parameter values (Table 2) were adjusted in an iterative manner to give the best statistical fit to the data ($r^2 = 0.77$).

Table 2
Physical parameters and master variables used in the model.

Parameter	Description	Value	Unit
z	Water depth	110	m
T	Bottom water temperature	286	K
S	Bottom water salinity	35.5	–
pH	Constant assumed pH	7.9	–
L	Length of modeled sediment core	515	cm
φ_0	Porosity at sediment-water interface	0.95	–
p	Partitioning coefficient of modeled porosity	0.89	–
x_{por1}	Porosity depth attenuation length	6.9	cm
x_{por2}	Porosity depth attenuation length	7385	cm
v	Sedimentation velocity	0.34	cm y^{-1}
ρ_s	Dry sediment density	1.42	g cm^{-3}
D_M^0	Sediment mixing rate at surface	100	cm^2 y^{-1}
x_{mix}	Halving depth of sediment mixing rate at surface	12	cm
x_T	Mixing attenuation length scale	1	cm
Φ_0	Non-local mixing rate at surface (for nitrate)	240	y^{-1}
x_Φ	Non-local exchange length scale (for nitrate)	5.13	cm

Dry sediment densities were calculated from the measured densities of the bulk sediment. The experimental data show a high degree of variation (Fig. 1b) and a mean value of 1.42 ± 0.46 g cm^{-3} was used in the model. This density is considerably lower than the density of lithogenic material (~2.5 g cm^{-3}) due to the high content of less-dense diatom opal and organic matter.

D_S (cm^2 y^{-1}) for each solute was calculated from the molecular diffusion coefficient in seawater (D_W, cm^2 y^{-1}) and the modeled porosity values (Boudreau, 1997; Schulz, 2000):

$$D_S = \frac{D_W}{1 - \ln \varphi^2} \quad (3)$$

Different diffusion coefficients were ascribed for the heavy and light isotopes of SO_4^{2-} and H_2S (Donahue et al., 2008), which makes a small overall difference to the isotope distributions and was included for completion.

Excess ^{210}Pb data ($^{210}Pb_{xs}$, Fig. 1c) from 0 to 14 cm depth visually indicate either physical reworking of the surface sediment or discontinuous ^{210}Pb initial activity and particle source flux. Assuming the former, mixing due to currents is probably more likely for this soupy organic-rich sediment rather than bioturbation, which was presumably absent because of bottom water anoxia. However, an isolated mixing event due to, for example, storm action cannot be unambiguously discounted. We are currently unable to definitively explain the ^{210}Pb data or the mode of surface sediment transport and mixing, and this caveat will be addressed in more detail in Section 4.1. Surface mixing was described using a depth-dependent rate function, D_M (cm^2 y^{-1}):

$$D_M = \frac{D_M^0}{2}\,\mathrm{erfc}\left(\frac{x - x_{mix}}{x_T}\right) \quad (4)$$

where D_M^0 is the mixing intensity at the sediment-water interface, x_{mix} is the depth where D_M equals half of D_M^0 and x_T is the characteristic depth scale over which the mixing decreases from full activity to zero. Fig. 1c shows simulation results for the $^{210}Pb_{xs}$ data using various mixing intensities. The data allow a range of 10–200 cm^2 y^{-1}, and 100 cm^2 y^{-1} was used for the baseline simulation.

The $^{210}Pb_{xs}$ data below 14 cm were used to quantify a sediment burial velocity of 0.34 cm y^{-1} using a semi-logarithmic transformation of $\ln(^{210}Pb_{xs})$ activity versus depth (Emeis et al., 2007) assuming that $^{210}Pb_{xs}$ is irreversibly particle bound. The derived value is of the same order as determined at other sites on the shelf and slope (~100 cm per 1000 y, Emeis et al., 2007).

A fundamental assumption in the model is that sulfide oxidation (SOx) in the surface sediments was mediated by *Thiomargarita* using NO_3^-, as occurs elsewhere where large sulfur bacteria are conspicuous (e.g. Fossing et al., 1995; Preisler et al., 2007). The mechanism by which *Thiomargarita* access the seawater NO_3^- reservoir is unknown. Unlike *Thioploca* and *Beggiatoa*, *Thiomargarita* are non-filamentous and chemotaxis through the sediment has not been observed. It has been postulated that NO_3^- regeneration of the cellular vacuoles occurs during sediment resuspension events (Schulz et al., 1999), although in Section 4.1 we

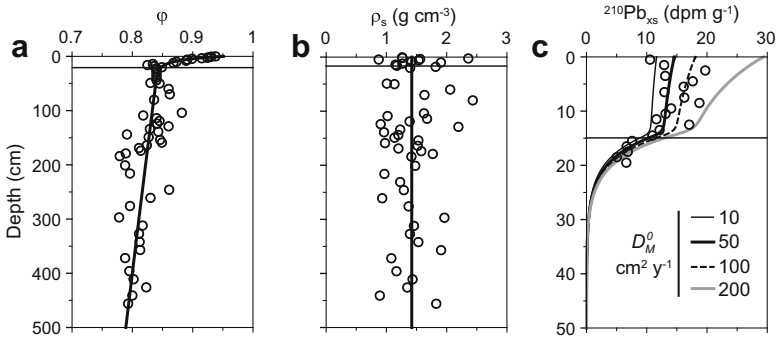

Fig. 1. Measured (symbols) and modeled (lines) depth profiles of (a) porosity (φ), (b) dry sediment density (ρ_s), and (c) $^{210}Pb_{xs}$ activity (note the different depth scale) with simulation results with different surface mixing intensities (D^0_M Eq. (4)). The flux of $^{210}Pb_{xs}$ to the surface (2 dpm g^{-1}) was calculated from the depth-integrated activity. No data were available below 20 cm. The horizontal lines indicate the depth of the mixed zone.

question this hypothesis. To approach the NO_3^- input pathway objectively, we assumed no a priori knowledge of how NO_3^- is transported into the sediment. Our intention was first to quantify the amount of NO_3^- required to reproduce the pore water H_2S data, assuming that the H_2S concentration in the surface layers is biogeochemically cycled mainly through SR and SOx. The results are then evaluated in Section 4.1 on the basis of the amount of NO_3^- required. A non-local source function (Φ) was used to describe the NO_3^- flux into the sediment:

$$\Phi = \Phi_0 \exp(x/x_\Phi) \quad (5)$$

where Φ_0 is the NO_3^- exchange rate at $x = 0$, and x_Φ is the depth attenuation length of exchange. This function is formally identical to that normally used to describe bioirrigation (solute exchange due to burrowing fauna) in 1D (e.g. Van Cappellen and Wang, 1996). In this application, Eq. (5) is not intended to represent bioirrigation because the bottom waters are anoxic, and the non-local exchange applies to NO_3^- only.

The boundary conditions at the sediment-water interface (C_0) were prescribed as fixed concentrations for solutes and fixed fluxes for solid species (Table 1). Solute concentrations were taken from the experimental data where possible. For NO_3^-, the upper boundary concentration (0.8 mM) was based on measured NO_3^- concentrations in *Thiomargarita* and total cell numbers as described in Section 2.6. A zero-gradient boundary condition ($\partial C/\partial x = 0$) was imposed for all species at the bottom of the model domain ($x = 515$ cm), so that transport through the lower boundary occurred exclusively by burial.

3.2. Reaction network

A conceptual diagram highlighting the major geochemical pathways and fractionations included in the model is shown in Fig. 2. Full details of the reaction network and rate expressions are provided in Table 3, and the corresponding biogeochemical parameters are listed in Table 4.

Following the multi-G model of Westrich and Berner (1984), POC deposited at the sediment-water interface was assumed to be comprised of 3 reactive fractions ('G_i') characterized by different first order rate constants, k_{Gi}; a fast reacting labile pool (G_1), a pool of intermediate reactivity (G_2) and a slowly reacting refractive pool (G_3). POC was degraded by dissimilatory iron reduction (r_{Fe}), sulfate reduction (r_{SR}) and methanogenesis (r_{ME}). The relative rate of each pathway was determined by a series of threshold concentrations akin to half-saturation constants (Table 3) and which follow Blackman kinetics (Van Cappellen and Wang, 1996).

The reactivity of G_1 and G_2 were determined from the measured rate of SR rather than from depth changes in POC concentration (Section 4.1). The reactivity of G_3, which was mainly decomposed by methanogenesis, was determined from the depth of free methane gas below the sea floor (4–5 m), as indicated by acoustic profiling (Emeis et al., 2004). Methane gas was produced when

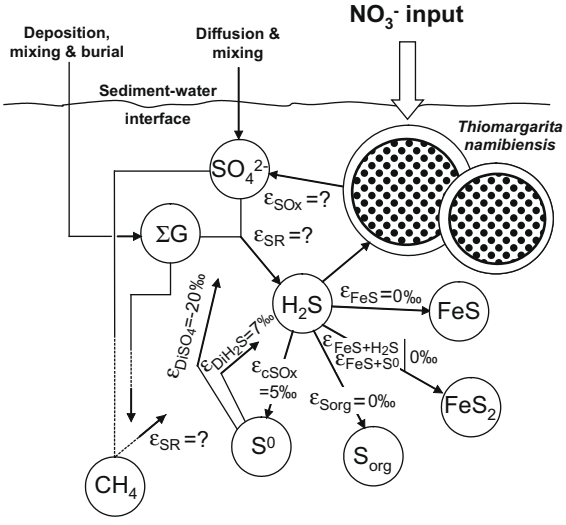

Fig. 2. Conceptual illustration of the main geochemical features at site 226680. The fractionations constrained with the model (ε_{SR} and ε_{SOx}) are indicated by '?'. *Thiomargarita* use sea water NO_3^- to oxidize H_2S to SO_4^{2-} which, in turn, can be used to oxidize organic carbon (G) or methane. A more detailed description of the reaction network is provided in Table 3.

Table 3
Reaction network and rate formulations included in the model. The sulfur concentration in the rate expressions corresponds to the total concentration (i.e. $r_i = {}^{32}r_i + {}^{34}r_i$). POC ('$G_i$') is assumed to consist of carbohydrate for mass balance calculations and also contains a fraction of reduced nitrogen ($(CH_2O)_1(NH_3)_{21/200}$). Three POC pools are considered (i.e. $POC = \Sigma G_i = G_1 + G_2 + G_3$). Dissolved inorganic carbon (DIC) species and alkalinity are not modeled explicitly, and for clarity the reactions are not proton balanced. DIC is reported as ΣCO_2.

r_i	Reaction	Rate expression
Kinetic processes		
r_{Fe}	$POC + 4Fe(OH)_{3-A} \rightarrow 4Fe^{2+} + \Sigma CO_2 + \frac{1}{21}NH_4^+ + 10H_2O$	$k_{Gi}\ POC\ f_{Fe}$
r_{SR}	$POC + \frac{1}{2}SO_4^{2-}; \rightarrow \frac{1}{2}H_2S + \Sigma CO_2 + \frac{1}{21}NH_4^+$	$k_{Gi}\ POC\ (1-f_{Fe})f_{SO_4}$
r_{ME}	$POC \rightarrow \frac{1}{2}CH_4 + \frac{1}{2}\Sigma CO_2 + \frac{1}{21}NH_4^+$	$k_{Gi}\ POC\ (1-SW_{SO_4})(1-(f_{Fe}+(1-f_{Fe})f_{SO_4}))$ $f_{Fe} = SW_{Fe} + (1\text{-}SW_{Fe})[Fe(OH)_{3\text{-}A}]/K_{Fe}$ $f_{SO_4} = SW_{SO_4} + (1\text{-}SW_{SO_4})[SO_4^{2-}]/K_{SO_4}$ $SW_{Fe} = 1$ if $[Fe(OH)_{3\text{-}A}] > K_{Fe}$ 0 if $[Fe(OH)_{3\text{-}A}] < K_{Fe}$ $SW_{SO_4} = 1$ if $[SO_4^{2-}] > K_{SO_4}$ 0 if $[SO_4^{2-}] < K_{SO_4}$
r_{hySR}	$SO_4^{2-} + 4H_2 \rightarrow H_2S + 4H_2O$	$k_{hySR}\ [H_2][SO_4^{2-}]$
r_{AOM}	$CH_4 + SO_4^{2-} \rightarrow H_2S + \Sigma CO_2 + 4H_2O$	$k_{AOM}\ [CH_4][SO_2^{2-}]$
r_{cSox}	$2Fe(OH)_{3\text{-(A or B)}} + H_2S + \rightarrow S^0 + Fe^{2+} + 6H_2O$	$k_{cSOx}[Fe(OH)_{3-(A\ or\ B)}][H_2S]^{0.5}$
r_{Di}	$S^0 + H_2O \rightarrow \frac{3}{4}H_2S + \frac{1}{4}SO_4^{2-}$	$k_{Di}[S^0]SW_{disp}$ $SW_{disp} = 1$ if $[H_2S] < [H_2S]^*$ 0 if $[H_2S] > [H_2S]^*$
r_{FeSp}	$Fe^{2+} + HS^- \rightarrow FeS$	$k_{FeSp}(\Omega_{FeS} - 1)SW_{FeS}$
r_{FeSd}	$FeS \rightarrow Fe^{2+} + HS^-$	$k_{FeSd}[FeS](1-\Omega_{FeS})(1-SW_{FeS})$
		$\Omega_{FeS} = ([Fe^{2+}][HS^-])/(10^{-pH}K_{FeS})$
		$HS^- = [H_2S]/(1+10^{-pH}K_{H_2S})$
		$SW_{FeS} = 1$ if $(\Omega_{FeS} - 1) > 1$ 0 if $(\Omega_{FeS} - 1) < 1$
$r_{FeS}+H_2S$	$FeS + H_2S \rightarrow FeS_2 + H_2$	$k_{FeS+H_2S}[FeS][H_2S]$
$r_{FeS} + S^0$	$FeS + S^0 \rightarrow FeS_2$	$k_{FeS+S^0}[FeS][S^0]$
r_{Sorg}	$(G_1 + G_2) + (H_2S) \rightarrow$ "G–H_2S"	$k_{Sorg}[G_1+G_2][H_2S]$
r_{SOx}	$H_2S + NO_3^- + H_2O \rightarrow SO_4^{2-} + NH_4^+$	$k_{SOx}[NO_3^-][H_2S]$
r_{gas}	$CH_{4(aq)} \rightarrow CH_{4(g)}$	$k_{gas}([CH_4] - [CH_4^*])SW_{gas}$
		$SW_{gas} = 1$ if $[CH_4] - [CH_4^*] > 1$ 0 if $[CH_4] - [CH_4^*] < 1$
Equilibrium processes		
r_{NH_4ads}	$NH_4^+ \leftrightarrow \equiv NH_4^+$	$[\equiv NH_4^+] = K_{NH_4ads}[NH_4^+]$
r_{Feads}	$Fe^{2+} \leftrightarrow \equiv Fe^{2+}$	$\equiv Fe^{2+} = K_{Feads}[Fe^{2+}]$

the dissolved methane (CH_4) concentration exceeded the in situ solubility concentration (CH_4^*; r_{gas}, Table 3). Free gas was not explicitly modeled. CH_4 diffusing upwards from depth was allowed to be consumed by anaerobic oxidation of methane (AOM) according to a bimolecular dependence on CH_4 and SO_4^{2-} (r_{AOM}, Van Cappellen and Wang, 1996).

Denitrification was not considered because, although NO_3^- is modeled as a solute, it is assumed to be confined within *Thiomargarita* cells and, therefore, not transported

Table 4
Biogeochemical parameters used in the baseline simulation. The source of the parameter values is indicated as follows: C, constrained with the model using the measured data; L, based on literature values; I, independently determined from field data. The literature sources are indicated in the table footnote.

Parameter	Description	Value	Unit	Source
k_{G_1}	Reactivity of POC pool G_1	2.0	y^{-1}	C
k_{G_2}	Reactivity of POC pool G_2	0.03	y^{-1}	C
k_{G_3}	Reactivity of POC pool G_3	1.4×10^{-4}	y^{-1}	C
k_{AOM}	Rate constant for AOM	10000	$M^{-1}\ y^{-1}$	L[1]
k_{cSOx}	Rate constant for chemical sulfide oxidation	0.1	†	C
k_{Di}	Rate constant for S^0 disproportionation	0.001	y^{-1}	L[2]
k_{FeSp}	Rate constant for FeS precipitation	1.5×10^{-7}	$M\ y^{-1}$	L[2,3]
k_{FeSd}	Rate constant for FeS dissolution	0.001	y^{-1}	L[3]
k_{FeS+S0}	Rate constant for FeS_2 precipitation with S^0	10,000	$mol^{-1}\ g\ y^{-1}$	L[3]
$k_{FeS+H2S}$	Rate constant for FeS_2 precipitation with H_2S	60,000	$M^{-1}\ y^{-1}$	C
k_{SOx}	Rate constant for microbial sulfide oxidation by NO_3^-	1.0×10^7	$M^{-1}\ y^{-1}$	C
k_{Sorg}	Rate constant for sulfidization of organic matter	0.2	$M^{-1}\ y^{-1}$	C
k_{gas}	Rate constant for CH_4 gas formation	1.0	y^{-1}	I
K_{SO_4}	Threshold concentration for SO_4^{2-}	100	μM	L[1]
K_{Fe}	Threshold concentration for $Fe(OH)_{3\text{-}A}$	2000	$\mu mol\ g^{-1}$	C
K_{FeS}	Stability constant for FeS	0.0063	M	L[1]
K_{Feads}	Fe^{2+} adsorption coefficient	400	–	L[1,4]
K_{NH4ads}	NH_4^+ adsorption coefficient	1.6	–	L[4]
K_{H2S}	Acidity constant for H_2S	2.48×10^{-7}	–	I
H_2S^*	Threshold H_2S concentration for disproportionation	10.0	mM	I
CH_4^*	In situ CH_4 solubility	18.0	mM	I
ε_{SR}	Rate-dependent fractionation factor	(Eq. (20))	‰	C
m_{SR}	Steepness of variability of ε_{SR} with rate	1.5	$mM^{-1}\ y$	C
$\varepsilon_{SR\text{-}max}$	Maximum imposed value of ε_{SR}	100	‰	C
ε_{cSOx}	Fractionation for chemical sulfide oxidation	5	‰	L[5]
ε_{DiSO4}	Fractionation for S^0 disproportionation to SO_4^{2-}	−20	‰	L[6]
ε_{DiH_2S}	Fractionation for S^0 disproportionation to H_2S	7	‰	L[6]
ε_{FeS}	Fractionation for FeS precipitation/dissolution	0	‰	L[4]
ε_{FeS+S0}	Fractionation for FeS_2 precipitation with FeS and S^0	0	‰	L[7]
$\varepsilon_{FeS+H2S}$	Fractionation for FeS_2 precipitation with FeS and H_2S	0	‰	L[7]
ε_{Sorg}	Fractionation for sulfidization of POC	0	‰	L[8]
ε_{SOx}	Fractionation for microbial sulfide oxidation with NO_3^-	25	‰	C

† Rate constant unit = g $(mol\ Fe)^{-1}\ L^{0.5}\ (mol\ H_2S)^{0.5}\ y^{-1}$.
[1] References: Van Cappellen and Wang (1996).
[2] Jourabchi et al. (2005).
[3] Meysman et al. (2003).
[4] Berg et al. (2003).
[5] Fry et al. (1988), Böttcher et al. (2001).
[6] Canfield and Thamdrup (1994).
[7] Price and Shieh (1979), Wilkin and Barnes (1996).
[8] Werne et al. (2003).

by molecular diffusion and unavailable for chemical reactions other than SOx. In addition, denitrification in *Thioploca*-bearing sediments has been shown previously to be of minor importance (Thamdrup and Canfield, 1996). The role of manganese oxide in POC mineralization was also ignored because manganese is highly depleted in Namibian sediments compared to the average shale (Borchers et al., 2005). The dominance of POC mineralization by SR (see Section 4.1) further justifies these omissions.

The reaction mechanism of SO_x is not fully understood (r_{SOx}, Table 3). The presence of intracellular S^0 globules suggests that oxidation may be a two-step process, as proposed for *Thioploca* (Fossing et al., 1995; Otte et al., 1999; Zopfi et al., 2001). However, SOx was initially described with a bimolecular rate law with respect to H_2S and NO_3^- to produce SO_4^{2-} directly (Table 3). This assumption is re-evaluated in Section 4.4.

Iron oxide minerals were modeled as a labile and a refractory fraction based on observations by Borchers et al. (2005), termed $Fe(OH)_{3\text{-}A}$ and $Fe(OH)_{3\text{-}B}$, respectively (Berg et al., 2003). The fluxes of these pools were determined by optimum model fit to the data. The labile fraction was available for dissimilatory reduction (r_{Fe}) and reduction by H_2S (r_{cSOx}) (referred to as chemical sulfide oxidation from here on) whereas $Fe(OH)_{3\text{-}B}$ was only available for chemical sulfide oxidation. The latter process produces S^0 (Böttcher et al., 2001) and was described using the rate expression determined experimentally by Poulton et al. (2004).

Adsorption of dissolved Fe^{2+} and NH_4^+ onto sediment particles was described as a reversible, linear equilibrium reaction (r_{Feads}, r_{NH4ads}, Table 3). Siderite precipitation is inhibited in the presence of H_2S (Haese, 2000) and is not considered in the model. Depending on the saturation state of the pore fluid, Fe^{2+} was consumed or produced through precipitation (r_{FeSp}) and dissolution (r_{FeSd}) of FeS, respectively. A constant pH of 7.9, measured at a similar site on the shelf, was imposed to calculate the FeS saturation index (data not shown). At this pH, 5% of total H_2S is present as dissolved hydrogen sulfide gas.

Precipitation of FeS to pyrite (FeS_2, r_{Fes+H_2S}) via the H_2S pathway or with elemental sulfur (S^0, r_{FeS+S0}) (Rickard and Luther, 2007) was formulated using bimolecular rate expressions (e.g. Berg et al., 2003). S^0 was also consumed by disproportionation to SO_4^{2-} and total H_2S (r_{Di}). Thamdrup et al. (1993) reported thermodynamic inhibition of disproportionation in Danish shelf sediments when total H_2S concentration exceeded >1 mM. In the mud belt, thermodynamic calculations (not shown) suggest that it becomes inhibited when total H_2S >10 mM, and this threshold was implemented in the model. This provides the microorganisms with ~10 kJ mol^{-1} of S^0, which is similar to the proposed minimum Gibbs energy threshold for anaerobic microbial activity (Hoehler, 2004). Finally, diagenetic sulfidization of organic matter by H_2S was included, using a bimolecular rate law (r_{Sorg}) dependent on the concentration of total H_2S and reactive POC.

3.3. Sulfur isotope systematics

Isotope compositions in this study (Fig. 2) are expressed in per mil (‰) in the standard δ notation relative to the Canyon Diablo Triolite (CDT = 0.0450045):

$$\delta^{34}S = \left(\frac{(^{34}S/^{32}S)_{sample}}{(^{34}S/^{32}S)_{VCDT}} - 1 \right) \cdot 1000 \quad (6)$$

where ^{32}S and ^{34}S are the concentrations of the light and heavy isotope, respectively. In addition, the isotope difference between two sulfur compounds, S_A and S_B, is reported as $\Delta^{34}S$:

$$\Delta^{34}S = \delta^{34}S_A - \delta^{34}S_B \quad (7)$$

The simulation of $\delta^{34}S$ was achieved by modeling ^{32}S and ^{34}S as separate species:

$$^{32}S_A \xrightarrow{^{32}K} {}^{32}S_B \quad (8)$$

$$^{34}S_A \xrightarrow{^{34}K} {}^{34}S_B \quad (9)$$

where ^{32}k and ^{34}k are the corresponding rate constants. Note that the isotope speciation of pyrite (FeS_2) has three components: $Fe^{32}S^{32}S$, $Fe^{34}S^{34}S$ and $Fe^{32}S^{34}S$. These are referred to as $Fe^{32}S_2$, $Fe^{34}S_2$, and $Fe^{32,34}S_2$, respectively.

For normal kinetic isotope effects, the light isotope reacts faster than the heavy isotope. The opposite is true for an inverse kinetic isotope effect. For a given reaction where sulfur is a reactant species, the rate of reaction, r_i (Table 3), is the sum of the rates for the individual isotopes:

$$r_i = {}^{32}r_i + {}^{34}r_i \quad (10)$$

$$^{32}r_i = {}^{32}k_i {}^{32}S \quad (11)$$

$$^{34}r_i = {}^{34}k_i {}^{34}S \quad (12)$$

The ratio of the rate constants is equal to the fractionation factor for that particular pathway (α_i):

$$\alpha_i = \frac{^{32}k}{^{34}k} \quad (13)$$

Rearrangement of Eqs. (10)–(13) gives the specific rates of isotope uptake:

$$^{32}r_i = r_i \frac{\alpha_i {}^{32}S}{{}^{34}S + \alpha_i {}^{32}S} \quad (14)$$

$$^{34}r_i = r_i \frac{{}^{34}S}{{}^{34}S + \alpha_i {}^{32}S} \quad (15)$$

The same methodology was followed for all other reactions involving sulfur. No fractionation ($\varepsilon = 0‰$) was imposed for the precipitation of iron (Price and Shieh, 1979; Wilkin and Barnes, 1996) and organic sulfides. A small fractionation of $\varepsilon_{cSOx} = 5‰$ ($\alpha_{cSOx} = 1.005$) was permitted for chemical sulfide oxidation (Böttcher et al., 2001).

The model also considered the fractionation accompanying disproportionation (r_{Di}, Table 3). Four expressions and two fractionation factors are required to describe the rate of production of $^{32}SO_4^{2-}$ ($^{32}r_{DiSO_4}$), $^{34}SO_4^{2-}$ ($^{34}r_{DiSO_4}$), $H_2{}^{32}S$ ($^{32}r_{DiH_2S}$) and $H_2{}^{34}S$ ($^{34}r_{DiH_2S}$):

$$^{32}r_{DiSO_4} = r_{Di}\eta \frac{\alpha_{DiSO_4} {}^{32}S^0}{{}^{32}S^0 + \alpha_{DiSO_4} {}^{32}S^0} \quad (16)$$

$$^{34}r_{DiSO_4} = r_{Di}\eta \frac{{}^{32}S^0}{{}^{34}S^0 + \alpha_{DiSO_4} {}^{32}S^0} \quad (17)$$

$$^{32}r_{DiH_2}S = r_{Di}\eta \frac{\alpha_{DiH_2S} {}^{32}S^0}{{}^{34}S^0 + \alpha_{DiH_2S} {}^{32}S^0} \quad (18)$$

$$^{32}r_{DiH_2}S = r_{Di}\eta \frac{{}^{34}S^0}{{}^{34}S^0 + \alpha_{DiH_2S} {}^{32}S^0} \quad (19)$$

where α_{DiSO4} (0.980) and α_{DiH2S} (1.007) are the fractionation factors for SO_4^{2-} and H_2S production, respectively, and η corresponds to the different stoichiometric coefficients for SO_4^{2-} and H_2S products in the rate expression (Table 3). These imposed fractionations ($\varepsilon_{DiSO4} = -20‰$ and $\varepsilon_{DiH2S} = 7‰$) agree with those determined experimentally by Canfield and Thamdrup (1994), and result in a preferential depletion in ^{32}S for SO_4^{2-} and enrichment in ^{32}S for H_2S relative to S^0.

The fractionations for SOx by *Thiomargarita* (ε_{SOx}) and SR (ε_{SR}) were not specified a priori and were constrained from the measured data (see Section 4.3). ε_{SR} applies to r_{SR}, r_{hySR} and r_{AOM}. Canfield (2001) observed an increase in ε_{SR} with a decrease in SR rates. Accordingly, ε_{SR} was made to be dependent on the rate of SR (mM y^{-1}) using a linear function:

$$\varepsilon_{SR} = \varepsilon_{SR\text{-}max} - m_{SR} r_i \quad (20)$$

where i = SR, hySR or AOM, m_{SR} controls the steepness of change of ε_{SR} with the rate, and $\varepsilon_{SR\text{-}max}$ is the maximum fractionation (attained at the lowest SR rate).

4. RESULTS AND DISCUSSION

4.1. Sediment geochemistry

Measured POC (ΣG) concentrations are not available in the surface sediments but, based on the total carbon concentration (TC, Fig. 3a), probably decrease from around 10–11% dry sediment weight at the surface to ~5% at the base of the core (Fig. 3a). The high POC concentrations are not unusual for the inner shelf (Inthorn et al., 2006) and arise from a combination of factors which favor organic matter preservation, that is, high primary productivity, shallow water depth (110 m) and anoxic bottom waters (Brüchert et al., 2003; Borchers et al., 2005). The model simulation of the POC data is satisfactory, with a mismatch between the model and measured data immediately below the mixed layer. On the other hand, the simulated mineralization rates (Fig. 3b) show a good correspondence with the measured SR rates within and below the mixed layer (Fig. 3c). The model indicates that the surface POC is mainly comprised of the G_2 (4%) and G_3 (6%) pools, with G_1 being <1% of the sediment dry weight (Fig. 3a). These compare to the relative mineralization fluxes of 54% (G_1), 35% (G_2) and 11% (G_3).

It is unfortunate that pore water metabolite concentrations (e.g. ΣCO_2, NH_4^+) are not available to confirm the down-core rates of carbon mineralization. As a system scale confirmation, the model computes a depth-integrated ΣCO_2 efflux rate from the sediment of ~12 mol m^{-2} y^{-1}, which is of the same magnitude as that reported for *Thioploca*-bearing sediments off Chile determined from bag incubations of surface sediment (19–39 mol m^{-2} y^{-1}; Thamdrup and Canfield, 1996). Additionally, the model predicts a NH_4^+ efflux of 6.5 mol m^{-2} y^{-1}, which compares to 2.5–5.1 mol m^{-2} y^{-1} in Chile. This comparison, whilst not a rigorous means of confirming the model output, provides some confidence that the organic matter mineralization rates are reasonable for this type of environment.

The measured rate of SR (21–100 mM y^{-1}, Fig. 3c) at site 226680 also compares well to similar areas (Ferdelman et al., 1999; Thamdrup and Canfield, 1996; see also Section 4.2). The surface SR rate is markedly high for passive margin sediments where externally-impressed fluid advection is absent, and is driven by the reactive G_1 pool ($k_{G_1} = 2\ y^{-1}$) which is completely oxidized within the mixed surface layer (0–14 cm). Thamdrup and Canfield (1996) calculated similar carbon reactivity (2.5–4.5 y^{-1}), with SR rates up to 6 times higher than those reported here. The less-reactive G_2 fraction is buried through the mixed layer and fuels the exponential decrease in SR rate below 15 cm (Fig. 3c). The G_3 pool is relatively unreactive and decreases in concentration by only 2% over the modeled sediment column. SR and methanogenesis account for 30% and 70% of G_3 remineralization, respectively. Integrated over the whole core, however, they are responsible for 96% and 4% of total POC (ΣG) degradation, respectively.

Despite the high rates of bacterial SR, SO_4^{2-} penetrates 120 cm into the sediment where it is consumed by AOM in the sulfate-methane transition zone (SMTZ, Fig. 4a and b). The maximum AOM peak of 1.6 mM y^{-1} is a typical value for marine sediments dominated by diffusive transport of methane to the SMTZ (e.g. Fossing et al., 2000). The simulated methane concentration exceeds the measured concentration at depth, which is explained by degassing upon core retrieval to atmospheric pressure (Fig. 4b). The model predicts that methane saturation at the in situ temperature and pressure conditions is reached at 480 cm (18 mM; Duan et al., 1992), which agrees with observations made by acoustic profiling (Emeis et al., 2004). Below this depth, the dissolved methane concentration is constant and further methane production feeds the gaseous phase.

The geochemistry of H_2S shows some remarkable features which are characteristic of Namibian shelf sediments inhabited by *Thiomargarita* (Brüchert et al., 2003). In the upper 6 cm, H_2S is present at low concentrations (<0.1 mM, Fig. 4c), despite intense SR and anoxic bottom waters ($O_2 < 3$ μM). The model thus suggests that H_2S diffusing up from below the mixed layer is almost completely consumed by *Thiomargarita* before it can escape the sediment. Brüchert et al. (2003) calculated a lower efficiency of SOx (4–51%) elsewhere on the shelf which may indicate that *Thiomargarita* are present in greater densities at site 226680 or are more efficient at oxidizing sulfide.

The modeled rate of SOx which is required to simulate the measured pore water H_2S concentration is shown

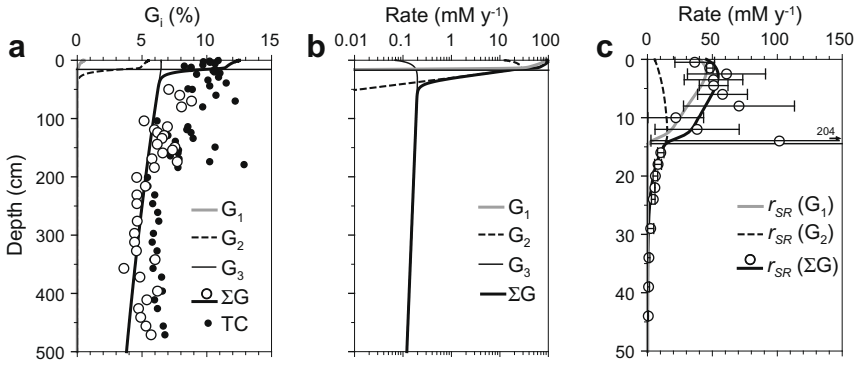

Fig. 3. Measured (symbols) and modeled (lines) depth profiles of (a) particulate organic carbon fractions (G_i) and total particulate carbon (TC), (b) rates of G_i remineralization (log scale), and (c) sulfate reduction rate. Note the different depth scale in (c) and that r_{SR} (G_3) is too low to be observed on the scale and is not shown. The horizontal lines indicate the depth of the mixed zone.

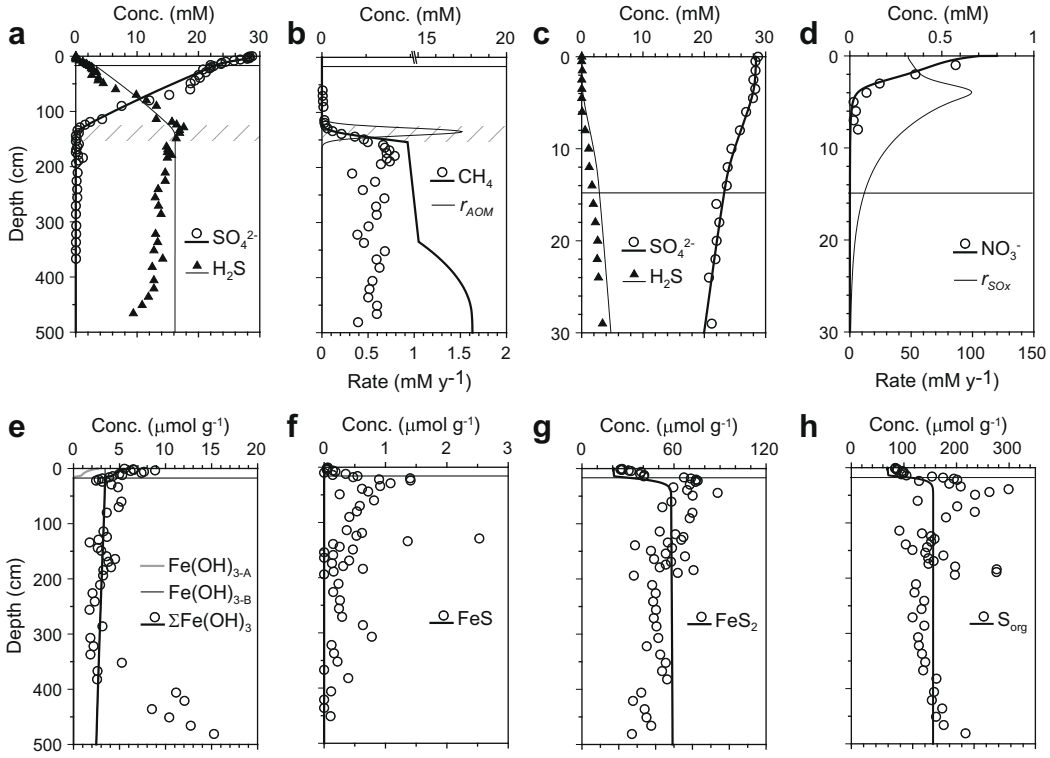

Fig. 4. Measured (symbols) and modeled (lines) depth profiles of (a) SO_4^{2-} and H_2S concentration, (b) methane concentration and AOM rate (r_{AOM}), (c) an enlargement of (a) over the top 30 cm, (d) pore water NO_3^- concentration calculated from intracellular NO_3^- concentrations and *Thiomargarita* cell numbers, and the rate of microbial sulfide oxidation (r_{SOx}), (e) labile ($Fe(OH)_{3\text{-}A}$) and refractory ($Fe(OH)_{3\text{-}B}$) iron oxide concentrations, (f) iron monosulfide concentration, (g) pyrite concentration, and (h) organic sulfur concentration. Note the *x*-axis break in (b) and the different depth scales for (c) and (d). The lower shaded area in (a) and (b) indicates the approximate extension of the SMTZ. The horizontal lines indicate the depth of the mixed zone.

in Fig. 4d, along with the NO_3^- estimated from *Thiomargarita* cell numbers and intracellular NO_3^- concentrations. The NO_3^- profile is qualitatively and quantitatively comparable to that estimated for *Thioploca*-containing sediments on the Chilean shelf (Zopfi et al., 2001), *Beggiatoa* mats in Eckernförde Bay (Preisler et al., 2007) and at other sites on the Namibian shelf. This provides some indication that the NO_3^- profile is representative of quasi-steady state. To reproduce the H_2S concentration just below the mixed zone (Fig. 4c), the model requires that SOx occurs to 20 cm depth, even though the observed *Thiomargarita* cell densities inferred from the NO_3^- concentration decrease rapidly in the top 10 cm (Fig. 4d). Filamentous *Beggiatoa* may be actively enhancing NO_3^- transport to the deeper layers at this site through their chemotactic behavior, but their biomass is much lower than *Thiomargarita* (Brüchert et al., 2006) and such a deep migration depth is questionable. The depth-integrated SOx rate and the sedimentary NO_3^- pool indicate a turnover time of only 2 days for NO_3^-, which compares to estimations of 4–50 days by Schulz and Jørgensen (2001). Currently, the mechanism by which *Thiomargarita* accesses the sea water nitrate is equivocal, but the rapid removal of NO_3^- demands an extremely effective transport mechanism if the H_2S data are characteristic of steady state conditions and no H_2S re-oxidation has occurred during sampling.

It has been hypothesized that sediment resuspension allows *Thiomargarita* to regenerate their NO_3^- reservoir from the sea water (Schulz and Jørgensen, 2001). The surface sediments at this site have been described as 'unusually fluid' (Schulz, 2002) and regular stirring of these layers by currents may allow *Thiomargarita* to contact the sea water. We were only able to create sufficient NO_3^- penetration into the sediment in the absence of additional non-local transport (Eq. (5)) using a minimum mixing rate of 10,000 $cm^2\ y^{-1}$ in Eq. (4) (data not shown); which is 40 times greater than typical in situ solute diffusion coefficients. It is difficult to imagine how such a strong mixing of the upper 12–15 cm of sediment can be achieved on a quasi-daily basis by current velocities which are only a few $cm\ s^{-1}$ at a height of 10 m above the sea floor (Mohrholz et al., 2008), whilst maintaining the geochemical gradients in the mixed layer. Furthermore, the deep location of free gas (4 m) likely rules out sediment resuspension due to mixing by protracted methane ebullition (Emeis et al., 2004; Haeckel et al., 2007). Admittedly, the mixing dynamics in the surface layer may be far more complex than can be computed by a 1D model, and this calls for short-term monitoring of the co-variance between sediment NO_3^- and H_2S concentrations and resuspension events. Without more information on the ecology of *Thiomargarita* and the abundance of *Beggiatoa* at this site, a definitive interpretation of the high NO_3^- turnover rate is not possible.

Accumulation of H_2S to high concentrations at depth (up to 15 mM) reflects the limited depositional flux and authigenic production of oxidants such as iron oxide, whose extremely low concentration (Fig. 4e) is exacerbated by biosiliceous dilution (Borchers et al., 2005). The data are best simulated using two iron oxide pools. $Fe(OH)_{3\text{-}A}$ decreases from 3 to 4 μmol g^{-1} at the sediment-water interface and is depleted by 16 cm. Borchers et al. (2005) also noted a very reactive iron oxide phase in dust originating from the nearby Namib Desert. The less-reactive $Fe(OH)_{3\text{-}B}$ phase is present at similar concentrations at the surface (4–5 μmol g^{-1}), but is poorly reactive over the entire sediment column. An increase in iron oxide concentration is observed below 400 cm, with maximum measured concentrations of 16 μmol g^{-1}. This deep iron-rich layer, which presumably originates from a geological change in depositional conditions, appears to be slowly drawing down the H_2S from the SMTZ causing a slight concentration decrease with depth (Fig. 4a). A much more pronounced H_2S drawdown occurs on the continental slope (Fossing et al., 2000), and has been observed in deep anoxic basins (e.g. Lyons et al., 2003; Jørgensen et al., 2004). However, the concentration profiles of FeS and FeS_2 (Fig. 4f and g) suggest that precipitation of downward diffusing H_2S to FeS_2 is insignificant.

FeS and FeS_2 are mostly formed in the upper 15 cm where the rate of iron oxide reduction is highest (Fig. 4f and g). FeS is present at very low concentrations throughout the core compared to other anoxic environments (e.g. Wijsman et al., 2001), with a peak of 1 μmol g^{-1} below the mixed zone which is not captured by the model. Wijsman et al. (2001) also observed a subsurface FeS peak in Black Sea sediments at 2–5 cm depth, which was interpreted as the depth of net FeS precipitation. Immediately below this depth the concentration of pyrite increased (Wijsman et al., 2001). In our model, however, FeS formation is rapid in the surface layers, which leads to concomitant FeS_2 precipitation (0.3% by weight). Borchers et al. (2005) also noted that pyritization is limited by the concentration of reactive iron in the mud belt and tends to be complete in the surface layers. Rapid pyritization in the Namibian sediments is probably favored by the mineral assemblage of iron and the high concentrations of H_2S and reactive POC (Raiswell and Canfield, 1998). A gradual decrease in measured FeS_2 concentration can be perceived below the mixed zone, which again may be indicative of a secular change in iron depositional flux with time.

Authigenic organic sulfur (S_{org}) constitutes a roughly equal amount to sedimentary sulfur as FeS_2 (Fig. 4h). Similarly high concentrations of S_{org} were observed on the Namibian continental slope (Fossing et al., 2000; Brüchert et al., 2000). Allochthonous sources of S_{org} probably account for ~1% of the POC mass and were not considered in the model. Like FeS_2, formation of S_{org} is extremely rapid at the surface. From the increase in S_{org} in the top layers, a first-order POC reactivity of 1.4×10^{-4} y^{-1} can be estimated, which is comparable to the value determined for the Cariaco Basin sediments (Werne et al., 2000). The decrease in SR rate below 50 cm depth (Fig. 3c) coincides with the observed peak in measured S_{org} concentration (200 μmol g^{-1}). These trends support the hypothesis of enhanced organic matter preservation through the formation of organic sulfur compounds with labile organic carbon (Sinninghe Damsté et al., 1989; Werne et al., 2004) and may even suggest a degree of competition for labile carbon. The subtle increase in S_{org} below 200 cm depth is also noteworthy because it contrasts with the decrease in FeS_2 concentration. Sulfidization of organic matter thus apparently continues at depth, albeit at much slower rates than in the surface layers. This observation is consistent with the low reactive iron concentration and supports the tenet that organic sulfur formation can occur when the reactive iron pool is depleted. Therefore, we may further hypothesize that the increase in dithionite-extractable iron at depth represents iron fractions that do not compete kinetically with functionalized organic compounds as a sink for H_2S.

4.2. Sulfur and iron dynamics

The model-derived depth-integrated mass balance (Fig. 5) shows that the SO_4^{2-} and H_2S dynamics are intensely dominated by SR and SOx. The model predicted SR rate (6100 mmol m^{-2} y^{-1}) is at the lower end of the range reported by Brüchert et al. (2003) for the Namibian shelf sediments (3–22 mol m^{-2} y^{-1}), yet it is twice the average value for upwelling systems quoted by Canfield et al. (2005). The H_2S produced by SR is re-oxidized by *Thiomargarita* back to SO_4^{2-} (6200 mmol m^{-2} y^{-1}), which significantly reduces the H_2S efflux to the water column (10 mmol m^{-2} y^{-1}, Fig. 4c). Astonishingly, only 2–3% of SO_4^{2-} input to the system occurs by transport across the sediment-water interface (160 mmol m^{-2} y^{-1}), with the remainder produced in situ by *Thiomargarita*. More than 96% of the SO_4^{2-} is used to mineralize POC and 4% (220 mmol m^{-2} y^{-1}) diffuses down to the SMTZ to be consumed by AOM. Thus, the intense oxidation of POC through SR, in addition to AOM, ultimately occurs with NO_3^- as the primary oxidant. Analogously, mass balance calculations for marine sediments underlying oxic bottom waters show that up to 90% of the H_2S produced is re-oxidized in situ at the expense of metal oxides and oxygen (Jørgensen, 1982).

A very different result is predicted if *Thiomargarita* activity ceases, which was tested by setting the rate of SOx to zero and allowing the model to return to steady-state conditions. Without SOx (Fig. 6), SO_4^{2-} penetration into the sediment dramatically decreases over time. After 100 years a new steady state is reached, and the depth of SO_4^{2-} penetration has shifted upwards by about 100 cm, making methane escape from the sediment a much more likely scenario. The increased proximity of methane to the sediment surface results from the higher fraction of the G_3 pool degraded by methanogenesis (92%) compared to the baseline simulation (31%). The pathway of G_1 and G_2 mineralization remains largely unaltered under these new conditions. The variable depth of free gas observed throughout the mud belt (Emeis et al., 2004) could, therefore, be related to the efficiency of SO_4^{2-} production by *Thiomargarita* or biomass concentration.

A small fraction of H_2S produced which is not oxidized by *Thiomargarita* (1%) is buried as H_2S, FeS_2 and S_{org}, with

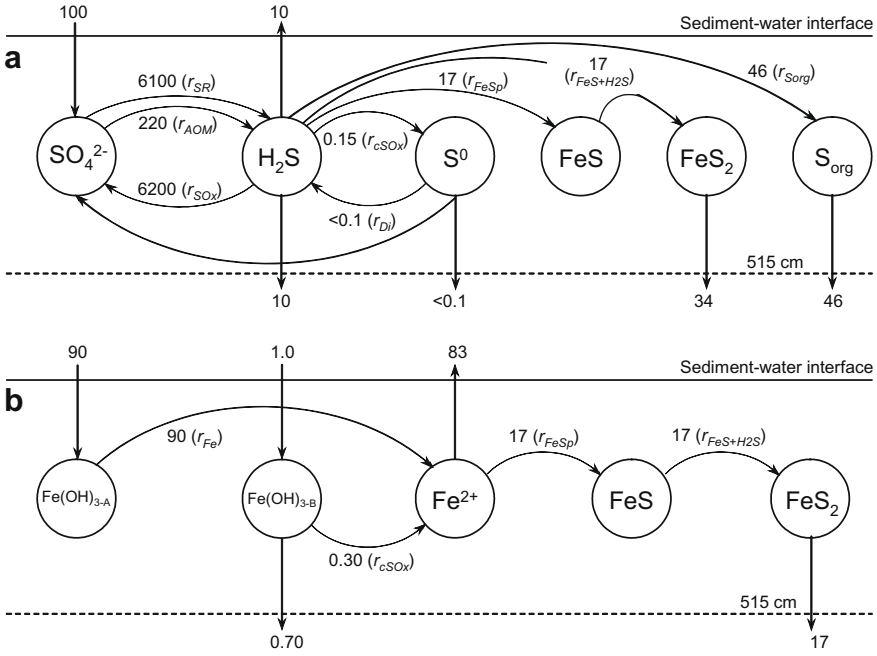

Fig. 5. Model-derived steady-state mass balance of (a) sulfur and (b) iron integrated over the upper 515 cm of sediment. Rates are given in mmol (S or Fe) $m^{-2}\,y^{-1}$ to two significant figures. Unless otherwise stated, rates less than 0.1 mmol $m^{-2}\,y^{-1}$ are not indicated. The stoichiometry of the reaction rates is provided in Table 3.

a negligible fraction oxidized to S^0 through chemical sulfide oxidation (Fig. 5a). Organic sulfur constitutes a greater burial sink than FeS_2 (46 versus 34 mmol $m^{-2}\,y^{-1}$), but note that the simulations for sedimentary sulfur diverge from the measured data at depth (Fig. 4g and h). The sulfur burial efficiency, defined as the ratio of the accumulation of sedimentary sulfur to the integrated rate of SR, is extremely low (<1%) due to the high rates of SR. Efficiencies of 10–20% can be considered to be more typical for marine sediments (Burdige, 2006), and values in this range have been calculated in deeper waters on the slope where SR rates are more than 10-fold lower (Ferdelman et al., 1999; Brüchert et al., 2000).

Labile iron oxide is completely reduced through dissimilatory iron reduction (90 mmol $m^{-2}\,y^{-1}$; Fig. 5b), yet this is only a minor pathway of total POC degradation (0.2%). Furthermore, chemical oxidation of refractive iron (0.3 mmol $m^{-2}\,y^{-1}$) is relatively trivial and most is buried. The low rate of chemical sulfide oxidation greatly reduces the potential for S^0 production. Consequently, disproportionation is 4 orders-of-magnitude lower (0.15 mmol $m^{-2}\,y^{-1}$) than the rate of SR and SOx (Fig. 5a). Disproportionation is thermodynamically inhibited when H_2S concentration exceeds 10 mM yet, in actuality, it is insensitive to this threshold concentration because of the shortage of oxidants. The potential for disproportionation is further limited by the anoxic bottom waters which preclude re-oxidation of reduced iron phases through sediment mixing. These re-oxidation pathways can be important in bioturbated sediments (e.g. Burdige, 1993). For example, re-oxidation of ferrous iron leads to integrated rates of iron reduction in the Skagerrak (Van Cappellen and Wang, 1996), Arctic (Berg et al., 2003) and pelagic sediments (Jourabchi et al., 2005) which are a factor of 3, 10 and 12 higher than the rate of iron oxide deposition, respectively. Disproportionation may have greater importance on the Namibian slope where bottom waters are perennially oxic (Brüchert et al., 2003).

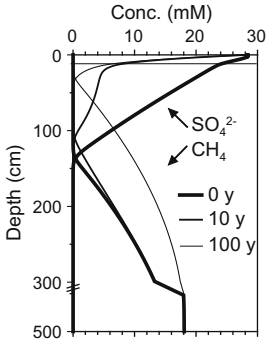

Fig. 6. Modeled evolution of the depth profiles of SO_4^{2-} and CH_4 concentration after setting the rate of sulfide oxidation (r_{SOx}) to zero. Steady-state is achieved after approximately 100 y. The horizontal line indicates the depth of the mixed zone.

4.3. Isotope dynamics

The isotope composition of SO_4^{2-} ($\delta^{34}S_{SO4}$) and H_2S ($\delta^{34}S_{H2S}$) at the study site (Fig. 7a) depend on their rate of addition and removal and the instantaneous fractionations during reactions. $\delta^{34}S_{SO4}$ increases with depth due to preferential removal of SO_4^{2-}, and shows an inflection at 24 cm at which point the $\delta^{34}S_{SO4}$ gradient becomes shal-

lower. At the base of the mixed layer, the modeled isotope difference between SO_4^{2-} and H_2S ($\Delta^{34}S$) reaches a maximum of 55‰, and then decreases with depth. In contrast, $\delta^{34}S_{H2S}$ decreases sharply from around 1‰ immediately below the sediment-water interface down to a minimum of −24‰ at 18 cm and then increases with depth. The model adequately captures these features by imposing a normal kinetic isotope effect for SOx (ε_{SOx}) by *Thiomargarita* of 25‰ and a normal kinetic isotope effect for SR (ε_{SR}, Eq. (20)) shown as the thick gray line in Fig. 7a. Values of $\varepsilon_{SR\text{-}max}$ and m_{SR} of 100‰ and 1.5 mM^{-1} y, respectively, are used in the calculation of ε_{SR}, which increases from 45‰ at the surface to 80‰ at 15 cm depth and to 100‰ at 30 cm depth.

Below the mixed layer, the baseline model shows a good correspondence to the measured $\delta^{34}S_{SO4}$ and $\delta^{34}S_{H2S}$ data (Fig. 7a). Average measured values for $\delta^{34}S_{H2S}$ and $\delta^{34}S_{SO4}$ at depths >100 cm are 16.0‰ and 57‰, respectively. There is a notable decrease in $\delta^{34}S_{H2S}$ beginning at around 40 cm which is not captured by the model and which also coincides with an inflection in the H_2S and SO_4^{2-} concentration data (Fig. 4a). We have no clear explanation for this feature, and cannot unambiguously rule out an episodic or an isolated bioirrigation event. The highest model fractionations for SR are expressed ($\varepsilon_{SR} = 100‰$) below the mixed layer because here the rates are lowest (Fig. 3c). At 50 cm depth (Fig. 7a), ε_{SR} is more than double the $\Delta^{34}S$ values of the measured data (40–50‰). This is a clear illustration of how differential diffusion of isotopes can engender a massive underestimation of the in situ fractionation if ε is simply equated to the Δ value inferred from geochemical profiles (i.e. assuming a closed system). Jørgensen (1979) and Chanton et al. (1987) provide a full discussion on this topic which will not be explored further here.

The model-derived fractionations ε_{SOx} and $\varepsilon_{SR\text{-}max}$, are far higher than previous laboratory-based estimates for these processes. Laboratory culture experiments suggest only small ($\varepsilon \approx <5‰$) fractionation during SOx by phototrophic bacteria (Fry et al., 1985, 1988), and one could argue that the data allow for a range of ε_{SOx} at the surface (15–35‰, Fig. 7b). Similarly, the maximum value observed for ε_{SR} in pure bacterial cultures is 47‰ (Brüchert, 2004), and our maximum value of 100‰ is 22‰ higher than the theoretical maximum equilibrium isotope fractionation at the in situ temperature (78‰, Farquhar et al., 2003). In a recent revision of the fractionation factors associated with the multi-stepped reduction of SO_4^{2-} in sulfate reducing bacteria, Brunner and Bernasconi (2005) showed that preferential back-flow of heavy H_2S to sulfite (SO_3^{2-}), rather simple expulsion of H_2S from the cell, allowed fractionations approaching these equilibrium values to be expressed. The fact that our model-constrained value exceeds this maximum fractionation may indicate that the model is missing a key process. As a qualitative sensitivity analysis, Fig. 7c shows the simulation results with $\varepsilon_{SR\text{-}max}$ values of 78‰ and 120‰, and illustrates that $\delta^{34}S_{SO4}$ and $\delta^{34}S_{H2S}$ are quite well constrained using $\varepsilon_{SR\text{-}max} = 100‰$. Furthermore, imposing the maximum experimentally-observed fractionation of 47‰ for $\varepsilon_{SR\text{-}max}$ completely fails to reproduce the observational data (Fig. 7d).

It is likely that SOx by large sulfur bacteria also occurs via intermediate chemical species (Dahl and Trüper, 1994). Some authors (e.g. Fossing et al., 1995) have suggested that globules of elemental sulfur (S^0) in the cell's cytoplasm represent the intermediate products of microbial sulfide oxidation. Theoretically, multi-stepped SOx would allow for the possibility of large fractionations in much the same way as for SR, yet it has not been verified experimentally and the metabolic details of the pathway remain to be fully investigated. The unusually high fractionation for SOx derived here is a primary new contribution of this study, but it

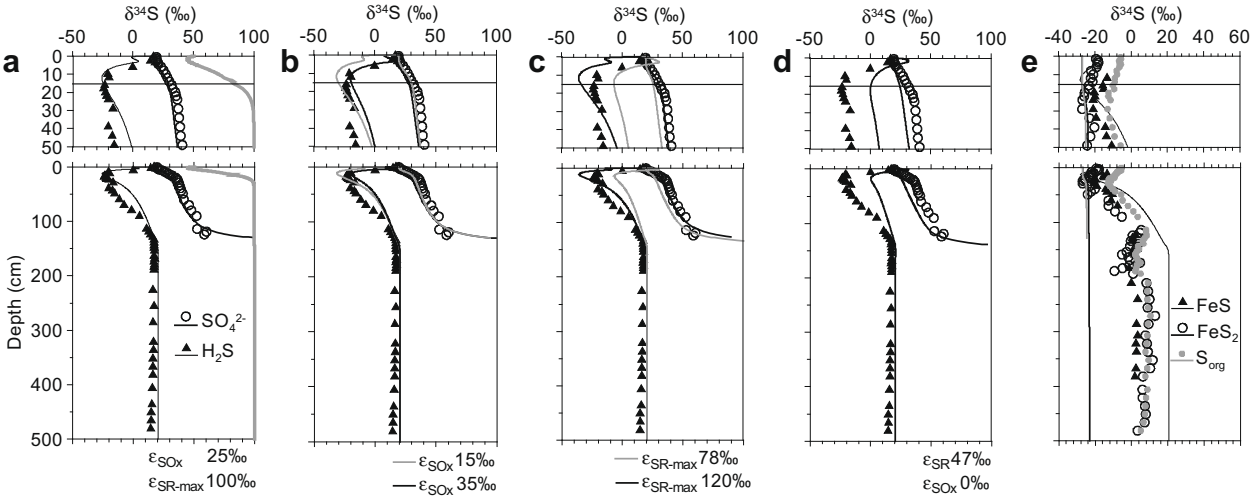

Fig. 7. Measured (symbols) and modeled (lines) sulfur isotope compositions. (a) baseline simulation showing SO_4^{2-} and H_2S using the parameter values in Table 4. The thick gray line shows the rate-dependent fractionation for sulfate reduction (ε_{SR}), (b) as in baseline, with $\varepsilon_{SOx} = 15‰$ and 35‰ (note that the two SO_4^{2-} curves are almost superimposed), (c) as in baseline, with $\varepsilon_{SR\text{-}max} = 78‰$ and 120‰, (d) as in baseline, with a fixed value of $\varepsilon_{SR} = 47‰$ throughout the sediment and $\varepsilon_{SOx} = 0‰$, and (e) baseline simulation showing FeS, FeS_2 and S_{org}. The top 50 cm of sediment are enlarged in the upper panels, where the horizontal lines indicate the depth of the mixed zone.

should be noted that it is uncorroborated by independent experimental data and subject to the assumption of the single-step SOx pathway (r_{SOx}, Table 3). The unusually high fractionations used to simulate the $\delta^{34}S_{SO4}$ and $\delta^{34}S_{H2S}$ data clearly warrant further analysis, and a critical examination of the SOx pathway in the next section suggests that much smaller values of ε_{SOx} are possible by assuming multi-stepped SOx.

The measured solid phase distributions of $\delta^{34}S_{Sorg}$, $\delta^{34}S_{FeS}$ and $\delta^{34}S_{FeS2}$ have minimum $\delta^{34}S$values of −13‰, −21‰ and −27‰ at 24 cm, respectively (Fig. 7e), and suggest an isotope discrimination by SR in the top layers of the sediments of up to 48‰ relative to sea water SO_4^{2-} (21‰). Even higher values of up to 65‰ have been noted elsewhere (Wijsman et al., 2001; Jørgensen et al., 2004). The model does not capture these trends, and the simulated $\delta^{34}S_{Sorg}$ and $\delta^{34}S_{FeS2}$ profiles are up to 30‰ lighter than the measured data, meaning that the actual amount of ^{34}S in FeS_2 and S_{org} is up to ~30% higher than predicted by the model. The modeled $\delta^{34}S_{FeS}$ is identical to that for $\delta^{34}S_{H2S}$.

The measured isotope abundances are unusual for two reasons. Firstly, FeS_2 is the most depleted of the solid species, which is indicative of fractionation during precipitation. The model assumes no fractionation during sulfide precipitation and the modeled $\delta^{34}S$ values of the authigenic phases are determined by mixing of the substrate reservoirs (Fossing and Jørgensen, 1990; Butler et al., 2004). The second feature corresponds to the relative change in concentrations and isotope distributions of the solid phases with depth. In the model, once sulfide precipitation is complete at around 20 cm, the $\delta^{34}S$ value is retained as it is progressively buried. FeS is an exception because it is a metastable species and its $\delta^{34}S$ value resembles $\delta^{34}S_{H2S}$. The measured data, in contrast, track the progressive enrichment of $\delta^{34}S_{H2S}$, concomitant with slightly decreasing concentrations (Fig. 4f and g). Down-core enrichment of FeS_2 and S_{org} in ^{34}S tends to be associated with sediments where diagenetic formation of sedimentary sulfur is ongoing (e.g. Werne et al., 2003). Somewhat similar trends in $\delta^{34}S_{FeS2}$ have been observed previously (Goldhaber and Kaplan, 1980; Wijsman et al., 2001; Jørgensen et al., 2004). Curiously, though, comparable isotope distributions at sites with abundant organic sulfur (Brüchert, 1998) and large sulfur bacteria (Zopfi et al., 2008) are absent, although the depth of sediment analyzed in these two studies may have been too shallow for the trends to materialize. Bacteria are known to accelerate mineral diagenesis (Donald and Southam, 1999), yet there are no obvious similarities or differences between these sites which can definitively indicate differential microbial alteration of the sulfide isotopes. The unusual parallel trends of the $\delta^{34}S$ profiles thus require an alternative explanation.

A hypothesis that could satisfy both the parallel isotope depth profiles and the relative isotope values relies on the idea of isotope exchange between H_2S and the solid phases. Exchange of sulfur between H_2S and FeS and S^0 through solubility-driven dissolution is relatively rapid (Fossing and Jørgensen, 1990). Yet, FeS_2 is only very sparingly soluble and likely does not exchange atoms with the surrounding porewater under typical marine conditions (Fossing and Jørgensen, 1990). Instead, we suggest that the extracted sulfur fractions (FeS, FeS_2, S_{org}) contain inert non-exchangeable sulfur and a portion of sulfur compounds associated with external mineral layers which can exchange sulfur from the ambient H_2S pool. Our reasoning relies on the fact that chemical extractions of sulfur compounds integrate mineralogically and compositionally distinct fractions (Brüchert and Pratt, 1996). For example, FeS_2 is most likely a composite of well-crystallized euhedral and framboidal pyrite, which are isotopically inhomogeneous (Morse, 1991; Canfield et al., 1992). Similar arguments apply to the acidic extraction of FeS (AVS), which is comprised of dissolved and solid sulfur complexes and mineral phases (Rickard and Morse, 2005).

To test this hypothesis in a theoretical context, we conducted a series of additional model simulations where the precipitation of the solid sulfur phase was accompanied by the co-precipitation of an exchangeable fraction following the same kinetics as in the baseline model. The total mass of the exchangeable and non-exchangeable fractions is equal to the total concentration of that phase, as before. The novel aspect of the new simulations is that the exchangeable fraction can reach isotope exchange equilibrium with the dissolved sulfide. Thus, by allowing exchange between discrete fractions of the solid rather than the entire pool, the heterogeneity in mineral structure was partially accounted for. The following equation describes the reaction taking place:

$$^{32}S - X.f_{ex} + H_2{}^{34}S \Longleftrightarrow {}^{34}S - X.f_{ex} + H_2{}^{32}S \quad (21)$$

where ^{32}S–X and ^{34}S–X are the total number of moles of ^{32}S and ^{34}S in compound X (FeS, FeS_2, S_{org}), and f_{ex} is the exchangeable fraction of the whole solid phase. This approach excludes the effects of changes in mineral composition and ageing with depth below the mixed layer after authigenic sulfur formation has ceased. A small fractionation factor during isotope exchange was imposed ($\varepsilon = 1.0‰$) (Price and Shieh, 1979; Wilkin and Barnes, 1996). f_{ex} is an adjustable model parameter which was varied until the best fit between the observations and model results was obtained, based on minimizing the root mean square error (RMSE(f_{ex})):

$$\mathrm{RMSE}(f_{ex}) = \sqrt{\frac{\sum_n ({}^{34}\delta_{obs} - {}^{34}\delta_{mod})}{n}} \quad (22)$$

where $^{34}\delta_{obs}$ and $^{34}\delta_{mod}$ are the observed and modeled values of $^{34}\delta_X$, respectively, and n is the number of paired data points. The baseline simulation was then re-run with the new exchange reactions. The results are shown in Fig. 8a for $^{34}\delta_{FeS2}$ and $^{34}\delta_{Sorg}$, which are obtained using a best fit f_{ex} value of 0.7. The inset in Fig. 8a shows that the values of f_{ex} giving similarly good fits to the data lie between 0.6 and 0.8, which means that 60–80% of the solid phase data undergoes exchange with dissolved sulfide from the pore water.

Although an exact fit to the data is not obtained, it is clear that the inclusion of an exchangeable fraction in the model provides a remarkably better simulation of the gen-

eral trends in the measured data. The corresponding profiles for $\delta^{34}S_{SO4}$ and $\delta^{34}S_{H2S}$ (Fig. 8b) remain essentially the same as before (Fig. 7a), presumably because of the small amount of the total solute pool which is exchanged (~μM) and the smoothing of the H_2S concentration profiles by transport processes. Isotope exchange with the dissolved and solid phases, if occurring, is thus insufficient to explain the large model-derived ε_{SR} values.

The presence of ^{34}S-enriched (e.g. 0.0‰ vs. CDT, Beier and Hayes, 1989) and ^{34}S-depleted pyrite (−48.2‰ vs. CDT) is known to be preserved in the ancient rock record (Ripley et al., 1990). Yet, significant diagenetic overprint of the solid phases would compromise the traditional interpretation of past benthic conditions and the long-term sedimentary $\delta^{34}S_{FeS2}$ record. At this site, the isotopic composition of buried sulfur is ~5 ‰. Such heavy values are generally viewed as igneous or hydrothermal in origin (Ohmoto and Goldhaber, 1997). Alternatively, Jørgensen et al. (2004) explain the presence of heavy pyrite in recent Black Sea sediments as the trapping of heavy dissolved sulfide into reactive iron layers below the zone of sulfate reduction. Black Sea sediments are unusual because the diagenetic alteration of iron mineral phases is an ongoing non-steady state effect originating from the increase in seawater salinity since the last glacial period. In this regard, the observation that the sediments become laminated below the mixed layer down to 120 cm at the present site may be significant (see Section 2.2). The laminations indicate that changes in sediment and bottom water geochemistry have occurred in the past, possibly resulting in ^{34}S-enrichment of sulfides

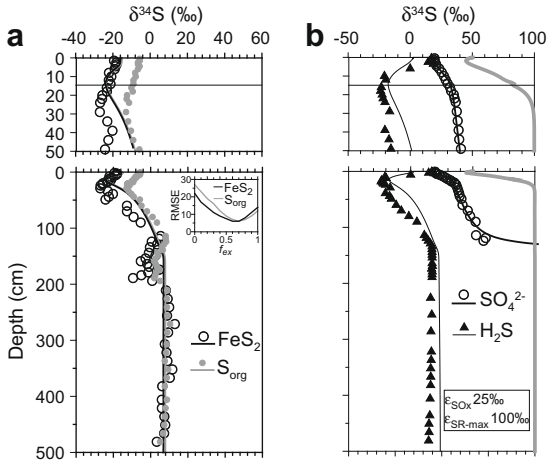

Fig. 8. Re-run of the baseline simulation with the inclusion of a fraction of the solid phase, f_{ex}, which reaches isotopic equilibrium with H_2S (Eq. (21)). (a) measured (symbols) and modeled (lines) sulfur isotopic compositions of total FeS_2 and S_{org}, (b) measured (symbols) and modeled (lines) sulfur isotopic compositions of SO_4^{2-} and H_2S. The thick gray line in (b) shows the rate-dependent fractionation for sulfate reduction (ε_{SR}). The model lines in (a) are almost superimposed and the inset shows the RMSE(f_{ex}) of the model fit to the data for different values of f_{ex} (Eq. (22)). The top 50 cm of sediment are enlarged in the upper panels, where the horizontal lines indicate the depth of the mixed zone.

due to a more restricted sulfate cycle (Jørgensen et al., 2004). The trigger for lamination is not known, and could be linked to a secular change in the anaerobic/dysaerobic state of the water column due to changes in primary productivity (Brüchert et al., 2000) or shelf circulation (Mohrholz et al., 2008). At this point, the relative interplay between long term changes in depositional conditions or biogeochemical isotope exchange phenomena is unclear, and our revised model simulations simply support a hypothetical scenario. Historic mass accumulation rates are required to help reconcile our analysis and provide further insight into the sedimentary sulfur geochemistry in Namibian shelf sediments.

4.4. Can multi-stepped sulfide oxidation and disproportionation explain the isotope distributions?

From the measured distributions of $\delta^{34}S_{H2S}$ and $\delta^{34}S_{SO4}$, a maximum fractionation for SR of around 100 ‰ was constrained with the model; more than double the maximum laboratory measured value of 47‰ and, to our knowledge, the highest value yet to be reported for sulfate reduction. Disproportionation (r_{Di}, Table 3) of sulfur compounds with an oxidation state intermediate between H_2S and SO_4^{2-} (e.g. S^0) is routinely proposed to explain apparent fractionations which are above 47‰ (Habicht and Canfield, 2001; Jørgensen et al., 2004). The general paradigm is founded on experiments (e.g. Canfield and Thamdrup, 1994) during which the H_2S produced by disproportionation is strongly depleted in ^{34}S and the SO_4^{2-} produced is correspondingly enriched in ^{34}S. Repeated cycles of H_2S re-oxidation back to S^0, followed by disproportionation of S^0 to H_2S and SO_4^{2-}, can ultimately lead to H_2S which is strongly depleted in ^{34}S. However, we reject this classical disproportionation hypothesis for site 226680 because, as mentioned previously, (i) there is a lack of allochthonous iron and manganese oxide in the sediment, (ii) there is reduced capacity for authigenic ferric iron precipitation due to bottom water column anoxia, and (iii) the rates of SR and SOx are orders-of-magnitude higher than the depositional iron oxide fluxes and exert a dominant control on the pore water profiles. Further model simulations (not shown) reveal that disproportionation has a negligible effect on the $\delta^{34}S$ profiles even when all the iron oxide is chemically reduced by H_2S to produce S^0.

Other authors have also discounted the disproportionation argument for different reasons. Rudnicki et al. (2001) and Wortmann et al. (2001) reported model-derived fractionation factors for SR of 77 ± 7‰ and 65‰, respectively. Rudnicki et al. (2001) attributed the high fractionations to low cell specific rates, reflecting increased substrate recalcitrance (Canfield, 2001). However, their rates were up to ~10^5 times lower than those reported here, which invalidates a similar interpretation of our data. Conversely, Wortmann et al. (2001) hypothesized that their data reflect the physiological trait of a hitherto uncultured sulfate reducing bacteria. Elaborating even further, Werne et al. (2003) ascribed high fractionations in Cariaco Basin sediments (65‰) to the activity of an unknown microbe carrying out an unknown pathway. Whilst we cannot rule

out these last two hypotheses for site 226680, they are not supported by empirical data.

An alternative pathway does exist which may permit authigenic iron oxide synthesis, and thus S^0 synthesis, in the absence of dissolved oxygen and manganese oxides. Geochemical profiles measured in sediment cores indicate that denitrification can be coupled to ferrous iron oxidation (Froelich et al., 1979; Straub et al., 1996):

$$10Fe^{2+} + 2NO_3^- + 24H_2O \rightarrow 10Fe(OH)_3 + N_2 + 18H^+ \quad (23)$$

This reaction was not included in the model because NO_3^- was assumed to be confined within *Thiomargarita* cells. However, re-running the baseline simulation including this reaction revealed no observable change to the $\delta^{34}S_{H2S}$ and $\delta^{34}S_{SO4}$ distributions (data not shown). This finding does not unambiguously rule out this reaction as the cause for the large $\Delta^{34}S$ because the biodiversity and microbial activity at this site has not been fully assayed. Instead, it supports the dominance of SR and SOx on the isotope profiles and, if denitrifying iron-oxidizing bacteria are present, then their overall impact on the sulfur geochemistry at this site is probably minor.

In a final application of the model, the assumption that SOx occurs as a single oxidation step is examined in more detail. We originally assumed that S^0 is a reactive intermediate in the oxidation of H_2S, which allowed SOx to be described as the sum of the two individual nitrate-using steps through the single step reaction (Eq. (26)):

$$\tfrac{1}{4}NO_3^- + H_2S + \tfrac{1}{2}H^+ \rightarrow S^0 + \tfrac{1}{4}NH_4^+ + \tfrac{3}{4}H_2O \quad (24)$$

$$\tfrac{3}{4}NO_3^- + S^0 + \tfrac{7}{4}H_2O \rightarrow SO_4^{2-} + \tfrac{3}{4}NH_4^+ + \tfrac{1}{2}H^+ \quad (25)$$

$$\text{Net}: \quad H_2S + NO_3^- + H_2O \rightarrow SO_4^{2-} + NH_4^+ \quad (26)$$

However, instead of being completely oxidized, S^0 may be disproportionated within the cell, giving the same net reaction:

$$NO_3^- + 4H_2S + 2H^+ \rightarrow 4S^0 + NH_4^+ + 3H_2O \quad (27)$$

$$4S^0 + 4H_2O \rightarrow 3H_2S + SO_4^{2-} + 2H^+ \quad (28)$$

$$\text{Net}: \quad H_2S + NO_3^- + H_2O \rightarrow SO_4^{2-} + NH_4^+ \quad (29)$$

The main difference between these pathways is that the disproportionation step (Eq. (28)) occurs with large and opposite fractionations in H_2S and SO_4^{2-}, whereas fractionation of S^0 during oxidation (Eq. (25)) is implicitly included in the value of ε_{SOx}. The baseline model was subsequently modified to include Eqs. (27) and (28) as separate reactions, and the S^0 was allowed to disproportionate as before using the same value for the rate constant as a first approximation (r_{Di}, Table 3). The optimal model solution to the $\delta^{34}S_{H2S}$ and $\delta^{34}S_{SO4}$ profiles is shown in Fig. 9b and reveals a similar simulation of the data as for the baseline simulation (Fig. 9a). Two additional modifications were made to the model to achieve this fit; (i) the maximum fractionation for SR ($\varepsilon_{SR\text{-}max}$) was reduced from 100 to 78‰ (gray line in Fig. 9b), which is equal to the equilibrium fractionation between H_2S and SO_4^{2-} at the in situ temperature (Farquhar et al., 2003), and (ii) the fractionation for SOx (ε_{SOx}) was reduced from 25‰ to 5‰, which is in agreement with laboratory measurements on sulfide-oxidizing bacteria (Fry et al., 1985, 1988). Note that the enrichment of $\delta^{34}S_{H2S}$ at the surface now occurs because of the opposing fractionation in H_2S and SO_4^{2-} during disproportionation rather than SOx, and a 5‰ value for ε_{SOx} is imposed because it produces a slightly better fit to the data than $\varepsilon_{SOx} = 0$‰.

This finding supports the idea that multi-stepped sulfide oxidation and disproportionation by *Thiomargarita* could be occurring at this site. Yet, because *Thiomargarita* has not been cultured experimentally, a definitive biogeochemical explanation which can be corroborated by empirical evidence is still lacking. It should also be remembered that the anomaly in the $\delta^{34}S_{H2S}$, H_2S and SO_4^{2-} data at 40 cm mentioned previously is unexplained and may be significant. On the other hand, the appearance of laminations down to 120 cm probably has less effect on the pore water isotope distributions since the time scale for diffusion to this depth (~100 y) is much less than the time for burial (~1000 y), implying that the solutes are in steady state. At this stage, it is worth remarking that anoxygenic phototrophic sulfide oxidation and S^0 disproportionation occur through very similar pathways and share a number of reactions, enzymes and intermediates including S^0 (Dahl and Trüper, 1994). In fact, the phototrophic sulfide oxidizer *Chlorobium* spp. can switch to the disproportionation pathway under conditions of low CO_2 concentration (Canfield et al., 2005). Detailed biochemical characterization of *Thiomargarita* and additional confirmation of the model against data collected at other sites in the mud belt will help to separate true microbial isotope fingerprints from possible model and analytical artifacts.

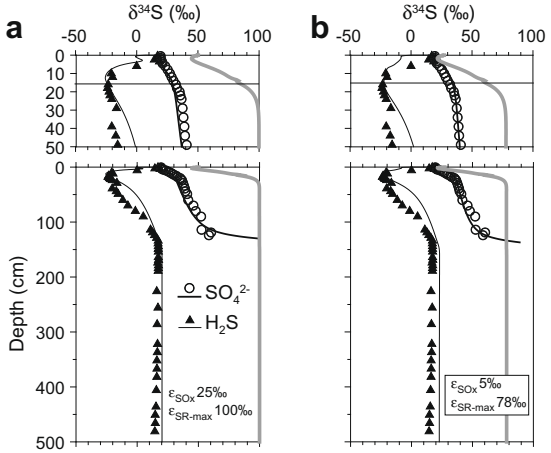

Fig. 9. Measured (symbols) and modeled (lines) sulfur isotope compositions and fractionations. (a) Baseline simulation results reproduced from Fig. 7(a) with $\varepsilon_{SR\text{-}max} = 100$‰ and $\varepsilon_{SOx} = 25$‰, (b) as baseline with $\varepsilon_{SR\text{-}max} = 78$‰ and $\varepsilon_{SOx} = 5$‰, yet now assuming that sulfide oxidation occurs via an intermediate (S^0) which is subsequently disproportionated (Eqs. (27)–(29)). The thick gray lines show the different rate-dependent fractionation for sulfate reduction (ε_{SR}) imposed in each case, and the horizontal lines indicate the depth of the mixed zone.

5. CONCLUSIONS

A reaction-transport model is applied to explore the interplay between the coupled C, N and S cycles at station 226680 in the Namibian mud belt. The sediment is hypersulfidic and is populated in the surface layers by the non-motile and non-filamentous bacteria *Thiomargarita namibiensis*, which thrives by oxidizing sulfide (H_2S) with internally-stored nitrate (NO_3^-). The key features of the study include an explicit model representation of stable sulfur isotope (^{32}S, ^{34}S) distributions which include sedimentary sulfides, and the incorporation of elemental sulfur disproportionation to isotopically distinct SO_4^{2-} and H_2S reaction products. The model simulation results are confirmed against an extensive geochemical data set including ^{32}S and ^{34}S relative abundances and the microbial NO_3^- content in the sediment estimated from *Thiomargarita* cell numbers and intracellular NO_3^- concentration.

The salient result from the modeling is that the sulfur cycle is completely dominated by coupled organoclastic sulfate reduction and microbial sulfide oxidation back to SO_4^{2-} by *Thiomargarita*. Furthermore, the oxidative-reductive sulfur cycle is almost entirely sustained by NO_3^- which is ultimately derived from the sea water. The presence of *Thiomargarita* has a broader indirect impact on the geochemistry at this site, because in situ SO_4^{2-} production pushes the sulfate-methane transition zone deeper into the sediment and helps prevent significant methane accumulation close to the sediment-water interface. The common belief that *Thiomargarita* access the sea water NO_3^- reservoir by resuspension of surface sediments induced by methane ebullition or bottom water currents is questionable at the present site and requires additional experimental verification.

The vertical isotope distributions allow key fractionations of the sulfur cycle to be extracted with the model including, for the first time, sulfide fractionation by *Thiomargarita*. As with previous modeling studies and for reasons which are still unclear at this stage, the model-derived fractionations for sulfate reduction are anomalously high compared to laboratory-based estimates. They do support, however, the recent paradigm of Brunner and Bernasconi (2005) and Johnston et al. (2007), in that sulfate reducing bacteria may fractionate in situ at values much closer to the equilibrium fractionation value than bacteria studied in the laboratory. The data also reveal a complex alteration of the isotope distribution in the solid sulfur phases during burial which is not easily reconciled from our current understanding of sedimentary sulfur geochemistry. A definitive explanation of these trends is not possible from the available data, and the role of isotope exchange with the dissolved sulfide pool remains an open question. However, a diagenetic overprint of the solid phases due to isotope exchange would compromise the current interpretation of the long-term sedimentary isotope record based on past benthic conditions. Reconciling this discrepancy is critical for a better interpretation of the historical sedimentary sulfur isotope record.

ACKNOWLEDGEMENTS

We thank Kay Emeis for the organization of Meteor cruise M48-2, Tim Ferdelman for the ^{210}Pb data, Peter Stief for the unpublished pH data, Tamara Zemskaya and Daniela Riechmann for the bacterial counts, and Andrea Schipper for assistance in the laboratory. We wish to express our gratitude to the Associate Editor (Robert Aller) and the three reviewers of this paper, Boz Wing, Filip Meysman, Matthias Haeckel, for their time and depth of constructive criticism which greatly improved this paper. We are also grateful to Philippe Van Cappellen and Paul Mason for insightful discussions. This work was financially supported by Netherlands Organization for Scientific Research (VIDI Grant no. 864.05.007), the Max-Planck Society, and the DFG priority program Auswertung von Meteorexpeditionen (Grant Jo 307/5-1).

APPENDIX A. SUPPLEMENTARY DATA

Supplementary data associated with this article can be found, in the online version, at doi:10.1016/j.gca.2008.12.015.

REFERENCES

Aguilera D. R., Jourabchi P., Spiteri C. and Regnier P. (2005) A knowledge-based reactive transport approach for the simulation of biogeochemical dynamics in Earth systems. *Geochem. Geophys. Geosyst.* **6**, Q07012. doi:10.1029/2004GC000899.

Bailey G. W., Beyers C. J. B. and Lipschitz S. R. (1985) Seasonal variation of oxygen deficiency in waters off southern south west Africa in 1975 and 1976 and its relation to the catchability and distribution of the cape rock lobster *Jasus lalandii*. *S. Afr. J. Mar. Sci.* **3**, 197–214.

Barlow R. G. (1982) Phytoplankton ecology in the southern Benguela current. I. Biogeochemical composition. *J. Exp. Mar. Biol. Ecol.* **63**, 209–227.

Beier J. A. and Hayes J. M. (1989) Geochemical and isotopic evidence for paleoredox conditions during deposition of the Devonian-Mississippian New Albany Shale, southern Indiana. *Geol. Soc. Am. Bull.* **101**, 774–782.

Berg P., Rysgaard S. and Thamdrup B. (2003) Dynamic modeling of early diagenesis and nutrient cycling. A case study in an Arctic marine sediment. *Am. J. Sci.* **303**, 905–955.

Berner R. A. (1980) *Early Diagenesis: A Theoretical Approach*. Princeton University Press, Princeton, p. 241.

Borchers S. L., Schnetger B., Böning P. and Brumsack H.-J. (2005) Geochemical signatures of the Namibian diatom belt: perennial upwelling and intermittent anoxia. *Geochem. Geophys. Geosyst.* **6**. doi:10.1029/2004GC000886.

Böttcher M. E., Thamdrup B. and Vennemann T. W. (2001) Oxygen and sulfur isotope fractionation during anaerobic bacterial disproportionation of elemental sulfur. *Geochim. Cosmochim. Acta* **65**, 1601–1609.

Boudreau B. P. (1997) *Diagenetic Models and Their Implementation: Modelling Transport and Reactions in Aquatic Sediments*. Springer, Verlag, Berlin, p. 414.

Braman R. S. and Hendricks S. A. (1989) Nanogram nitrite and nitrate determination in environmental and biological materials by vanadium (III) reduction with chemoluminescence detection. *Anal. Chem.* **61**, 71–88.

Bremner J. M. (1980) Physical parameters of the diatomaceous mud belt off South West Africa. *Mar. Geol.* **34**, M67–M76.

Brunner B. and Bernasconi S. M. (2005) A revised isotope fractionation model for dissimilatory sulfate reduction in sulfate reducing bacteria. *Geochim. Cosmochim. Acta* **69**, 4759–4771.

Brüchert V. (1998) Early diagenesis of sulfur in estuarine sediments: the role of sedimentary humic and fulvic acids. *Geochim. Cosmochim. Acta* **62**, 1567–1586.

Brüchert V. (2004) Physiological and ecological aspects of sulfur isotope fractionation during bacterial sulfate reduction. In *Sulfur Biogeochemistry – Past and Present*, vol. 379 (eds. A. P. Amend, K. J. Edwards and T. W. Lyons). Geological Society of America, pp. 1–16.

Brüchert V. and Pratt L. M. (1996) Contemporaneous early diagenetic formation of organic and inorganic sulfur in estuarine sediments from St. Andrew Bay, Florida, USA. *Geochim. Cosmochim. Acta* **60**, 2325–2332.

Brüchert V., Elena Pérez M. and Lange C. B. (2000) Coupled primary production, benthic foraminiferal assemblage, and sulfur diagenesis in organic-rich sediments of the Benguela upwelling system. *Mar. Geol.* **163**, 27–40.

Brüchert V., Jørgensen B. B., Neumann K., Riechmann D., Schlösser M. and Schulz H. (2003) Regulation of bacterial sulfate reduction and hydrogen sulfide fluxes in the central Namibian coastal upwelling zone. *Geochim. Cosmochim. Acta* **67**, 4505–4518.

Brüchert V., Currie B., Peard K. R., Lass U., Endler R., Dübecke A., Julies E., Leipe T. and Zitzmann S. (2006) An integrated assessment of shelf anoxia and water column hydrogen sulphide in the Benguela coastal upwelling system off Namibia. In *Past and Present Marine Water Column Anoxia* (ed. L. N. Neretin). Springer, pp. 161–194.

Burdige D. J. (1993) The biogeochemistry of manganese and iron reduction in marine sediments. *Earth-Sci. Rev.* **35**, 249–284.

Burdige D. J. (2006) *Geochemistry of Marine Sediments*. Princeton University Press, Princeton, p. 609.

Butler I. B., Böttcher M. E., Rickard D. and Oldroyd A. (2004) Sulfur isotope partitioning during experimental formation of pyrite via the polysulfide and hydrogen sulfide pathways: implications for the interpretation of sedimentary and hydrothermal pyrite isotope records. *Earth Planet. Sci. Lett.* **228**, 495–509.

Canfield D. E. (2001) Isotope fractionation by natural populations of sulfate-reducing bacteria. *Geochim. Cosmochim. Acta* **65**, 1117–1124.

Canfield D. E. and Thamdrup B. (1994) The production of ^{34}S-depleted sulfide during bacterial disproportionation of elemental sulfur. *Science* **266**, 1973–1975.

Canfield D. E., Raiswell R. and Bottrell S. (1992) The reactivity of sedimentary iron minerals toward sulfide. *Am. J. Sci.* **292**, 659–683.

Canfield D. E., Thamdrup B. and Kristensen E. (2005) Aquatic geomicrobiology. *Adv. Mar. Biol.* **48**, 640.

Chanton J. P., Martens C. S. and Goldhaber M. B. (1987) Biogeochemical cycling in an organic-rich coastal marine basin. 8. A sulfur isotopic budget balanced by differential diffusion across the sediment-water interface. *Geochim. Cosmochim. Acta* **51**, 1201–1208.

Chapman P. and Shannon L. V. (1985) The Benguela ecosystem Part II. Chemistry and related processes. *Oceanogr. Mar. Biol. Ann. Rev.* **23**, 183–251.

Cline J. D. (1969) Spectrophotometric determination of hydrogen sulfide in natural waters. *Limnol. Oceanogr.* **14**, 454–459.

Dahl C. and Trüper H. G. (1994) Enzymes of dissimilatory sulfide oxidation in phototrophic sulfur bacteria. *Methods Enzymol.* **243**, 400–412.

Donahue M. A., Werne J. P., Meile C. and Lyons T. W. (2008) Modeling sulfur isotope fractionation and differential diffusion during sulfate reduction in sediments of the Cariaco Basin. *Geochim. Cosmochim. Acta* **72**, 2287–2297.

Donald R. and Southam G. (1999) Low temperature anaerobic bacterial diagenesis of ferrous monosulfide to pyrite. *Geochim. Cosmochim. Acta* **63**, 2019–2023.

Duan Z., Moller N., Greenberg J. and Weare J. H. (1992) The prediction of methane solubility in natural waters to high ionic strength from 0 degrees to 250 degrees and from 0 to 1600 bar. *Geochim. Cosmochim. Acta* **56**, 1451–1460.

Emeis, K.-C., Bening, G., Berger, J., Brüchert, V., Currie, B., Endler, R., Ferdelman, T., Finke, N., Graco, M., Haferburg, G., Heyn, T., Kiessling, A., Lage, S., Leipe, T., Mollenhauer, G., Neumann, K., Nickel, G., Noli, K., Riechmann, D., Schippers, A., Schneider, R., Schulz, H., Shidjuu, A., Sonnabend, H., Stregel, S., Struck, U., Treppke, U., Vogt, T., Zemskaya, T., 2002. *Cruise Report Meteor Expedition M48-2, Walvis Bay - Walvis Bay, August 5–August 23*, 2000. University of Hamburg, Hamburg.

Emeis K.-C., Brüchert V., Currie B., Endler R., Ferdelman T., Kiessling A., Leipe T., Noli-Peard K., Struck U. and Vogt T. (2004) Shallow gas in shelf sediments of the Namibian coastal upwelling ecosystem. *Cont. Shelf Res.* **24**, 627–642.

Emeis, K.-C., Struck, U., Leipe, T., Ferdelman, T.G., 2007. Variability in upwelling intensity and nutrient regime in the coastal upwelling system offshore Namibia: results from sediment archives. *Int. J. Earth Sci.* 10.1007/s00531-007-0236-5.

Farquhar J., Johnston D. T., Wing B. A., Habicht K. S., Canfield D. E., Airieau S. and Thiemens M. H. (2003) Multiple sulphur isotopic interpretations of biosynthetic pathways: implications for biological signatures in the sulphur isotope record. *Geobiology* **1**, 27–36.

Ferdelman T. G., Lee C., Pantoja S., Harder J., Bebout B. M. and Fossing H. (1997) Sulfate reduction and methanogenesis in a Thioploca-dominated sediment off the coast of Chile. *Geochim. Cosmochim. Acta* **61**, 3065–3079.

Ferdelman T. G., Fossing H., Neumann K. and Schulz H. D. (1999) Sulfate reduction in surface sediments of the southeast Atlantic continental margin between 15°38'S and 27°57'S (Angola and Namibia). *Limnol. Oceanogr.* **44**, 650–661.

Fossing H. and Jørgensen B. B. (1989) Measurement of bacterial sulfate reduction in sediments: Evaluation of a single step chromium reduction method. *Biogeochemistry* **8**, 205–222.

Fossing H. and Jørgensen B. B. (1990) Isotope exchange reactions with radiolabeled sulfur compounds in anoxic seawater. *Biogeochemistry* **9**, 223–245.

Fossing H., Gallardo V. A., Jørgensen B. B., Hüttel M., Nielsen L. P., Schulz H., Canfield D. E., Glud R. N., Gundersen J. K., Küver J., Ramsing N. B., Teske A., Thamdrup B. and Ulloa O. (1995) Concentration and transport of nitrate by the mat-forming sulphur bacterium Thioploca. *Nature* **274**, 713–715.

Fossing H., Ferdelman T. G. and Berg P. (2000) Sulfate reduction and methane oxidation in continental margin sediments influenced by irrigation (South–East Atlantic off Namibia). *Geochim. Cosmochim. Acta* **64**, 897–910.

Froelich P. N., Klinkhammer G. P., Bender M. L., Luedtke N. A., Heath G. R., Cullen D. and Dauphin P. (1979) Early oxidation of organic matter in pelagic sediments of the eastern equatorial Atlantic: suboxic diagenesis. *Geochim. Cosmochim. Acta* **43**, 1075–1090.

Fry B., Gest H. and Hayes J. M. (1985) Isotope effects associated with the anaerobic oxidation of sulfite and thiosulfate by the photosynthetic bacterium, Chromatium vinosum. *FEMS Microbiol. Lett.* **27**, 227–232.

Fry B., Gest H. and Hayes J. M. (1988) $^{34}S/^{32}S$ fractionation in sulfur cycles catalyzed by anaerobic bacteria. *App. Environ. Microbiol.* **54**, 250–256.

Goldhaber M. B. and Kaplan I. R. (1980) Mechanisms of sulfur incorporation and isotope fractionation during early diagenesis in sediments of the Gulf of California. *Mar. Chem.* **9**, 95–143.

Habicht K. S. and Canfield D. E. (2001) Isotope fractionation by sulfate-reducing natural populations and the isotopic composition of sulfide in marine sediments. *Geology* **29**, 555–558.

Haeckel M., Boudreau B. P. and Wallmann K. (2007) Bubble-induced porewater mixing: a 3D model for deep porewater irrigation. *Geochim. Cosmochim. Acta* **71**, 5135–5154.

Haese R. R. (2000) The reactivity of iron. In *Geochemistry* (eds. H. D. Schulz and M. Zabel Marine). Springer-Verlag, Berlin, pp. 233–261.

Hoehler T. M. (2004) Biological energy requirements as quantitative boundary conditions for life in the subsurface. *Geobiology* **2**, 205–215.

Inthorn M., Wagner T., Scheeder G. and Zabel M. (2006) Lateral transport controls distribution, quality, and burial of organic matter along continental slopes in high-productivity areas. *Geology* **34**, 205–208.

Johnston D. T., Farquhar J. and Canfield D. E. (2007) Sulfur isotope insights into microbial sulfate reduction: When microbes meet models. *Geochim. Cosmochim. Acta* **71**, 3919–3947.

Jørgensen B. B. (1978) A comparison of methods for the quantification of bacterial sulfate reduction in coastal marine sediments: I. Measurement with radiotracer techniques. *Geomicrobiol. J.* **1**, 11–27.

Jørgensen B. B. (1982) Mineralization of organic matter in the sea bed – the role of sulphate reduction. *Nature* **296**, 643–645.

Jørgensen B. B. (1979) A theoretical model of the stable sulfur isotope distribution in marine sediments. *Geochim. Cosmochim. Acta* **43**, 363–374.

Jørgensen B. B., Böttcher M. E., Holger L., Neretin L. N. and Volkov I. I. (2004) Anaerobic methane oxidation and a deep H_2S sink generate isotopically heavy sulfides in Black Sea sediments. *Geochim. Cosmochim. Acta* **68**, 2095–2118.

Jourabchi P., Van Cappellen P. and Regnier P. (2005) Quantitative interpretation of pH distributions in aquatic sediments: a reaction-transport modeling approach. *Am. J. Sci.* **305**, 919–956.

Kalanetra K. M., Joye S. B., Sunseri N. R. and Nelson D. C. (2005) Novel vacuolate sulfur bacteria from the Gulf of Mexico reproduce by reductive division in three dimensions. *Environ. Microbiol.* **7**, 1451–1460.

Kostka J. E. and Luther G. W. (1994) Partitioning and speciation of solid phase iron in saltmarsh sediments. *Geochim. Cosmochim. Acta* **58**, 1701–1710.

Lyons T. W., Werne J. P., Hollander D. J. and Murray R. W. (2003) Contrasting sulfur geochemistry and Fe/Al and Mo/Al ratios across the last oxic-to-anoxic transition in the Cariaco Basin, Venezuela. *Chem. Geol.* **195**, 131–157.

Meysman F. J. R., Middelburg J. J., Herman P. M. J. and Heip C. H. R. (2003) Reactive transport in surface sediments. II. Media: an object-oriented problem-solving environment for early diagenesis. *Comp. Geosci.* **29**, 301–318.

Mohrholz V., Bartholomae C. H., van der Plas A. K. and Lass H. U. (2008) The seasonal variability of the northern Benguela undercurrent and its relation to the oxygen budget on the shelf. *Cont. Shelf Res.* **28**, 424–441.

Monteiro P. M. S., Nelson G., van der Plas A., Mabille E., Bailey G. W. and Klingelhoeffer E. (2005) Internal tide—shelf topography interactions as a forcing factor governing the large-scale distribution and burial fluxes of particulate organic matter (POM) in the Benguela upwelling system. *Cont. Shelf Res.* **25**, 1864–1876.

Morse J. W. (1991) Oxidation kinetics of sedimentary pyrite in seawater. *Geochim. Cosmochim. Acta* **55**, 3665–3667.

Ohmoto H. and Goldhaber M. B. (1997) Sulfur and carbon isotopes. In *Geochemistry of Hydrothermal Ore Deposits* (ed. H. L. Barnes). Wiley, New York, pp. 517–612.

Otte S., Kuenen J. G., Nielsen L. P., Paerl H. W., Zopfi J., Schulz H. N., Teske A., Strotmann B., Gallardo V. A. and Jørgensen B. B. (1999) Nitrogen, carbon, and sulfur metabolism in natural Thioploca samples. *App. Environ. Microbiol.* **65**, 3148–3157.

Poulton S. W., Krom M. D. and Raiswell R. (2004) A revised scheme for the reactivity of iron (oxyhydr)oxide minerals towards dissolved sulfide. *Geochim. Cosmochim. Acta* **68**, 3703–3715.

Preisler A., de Beer D., Lichtschlag A., Lavik G., Boetius A. and Jørgensen B. B. (2007) Biological and chemical sulfide oxidation in a Beggiatoa inhabited marine sediment. *ISME J.* **1**, 341–353.

Price F. T. and Shieh Y. N. (1979) Fractionation of sulfur isotopes during laboratory synthesis of pyrite at low temperatures. *Chem. Geol.* **27**, 245–253.

Raiswell R. and Canfield D. E. (1998) Sources of iron for pyrite formation in marine sediments. *Am. J. Sci.* **298**, 219–245.

Rickard D. and Luther, III, G. W. (2007) Chemistry of iron sulfides. *Chem. Rev.* **107**, 514–562.

Rickard D. and Morse J. W. (2005) Acid volatile sulfide (AVS). *Mar. Chem.* **97**, 206–212.

Ripley E. M., Shaffer N. R. and Gilstrap M. S. (1990) Distribution and geochemical characteristics of metal enrichment in the New Albany Shale (Devonian-Mississippian), Indiana. *Econ. Geol.* **8**, 1790–1807.

Rudnicki M. D., Elderfield H. and Spiro B. (2001) Fractionation of sulfur isotopes during bacterial sulfate reduction in deep ocean sediments at elevated temperatures. *Geochim. Cosmochim. Acta* **65**, 777–789.

Schulz H. D. (2000) Quantification of early diagenesis: Dissolved constituents in marine pore water. In *Marine Geochemistry* (eds. H. D. Schulz and M. Zabel). Springer-Verlag, Berlin, pp. 85–128.

Schulz H. N. (2002) Thiomargarita namibiensis: giant microbe holding its breath. *Am. Soc. Microbiol.* **68**, 122–127.

Schulz H. N. and Jørgensen B. B. (2001) Big bacteria. *Ann. Rev. Microbiol.* **55**, 105–137.

Schulz H. N., Brinkhoff T., Ferdelman T. G., Hernández Mariné M., Teske A. and Jørgensen B. B. (1999) Dense populations of a giant sulfur bacterium in Namibian shelf sediments. *Science* **284**, 493–495.

Sinninghe Damsté J. S., Rijpstra W. I. C., Kock-vanDalen A. C., De Leeuw J. W. and Schenck P. A. (1989) Quenching of labile functionalised lipids by inorganic sulphur species: evidence for the formation of sedimentary organic sulphur compounds at the early stages of diagenesis. *Geochim. Cosmochim. Acta* **53**, 1343–1355.

Stookey L. L. (1970) Ferrozine – a new spectrophotometric reagent for iron. *Anal. Chem.* **42**, 779–781.

Straub K. L., Benz M., Schink B. and Widdel F. (1996) Anaerobic, nitrate-dependent microbial oxidation of ferrous iron. *App. Environ. Microbiol.* **62**, 1458–1460.

Thamdrup B. and Canfield D. E. (1996) Pathways of carbon oxidation in continental margin sediments off central Chile. *Limnol. Oceanogr.* **41**, 1629–1650.

Thamdrup B., Finster K., Hansen J. W. and Bak F. (1993) Bacterial disproportionation of elemental sulfur coupled to

chemical reduction of iron or manganese. *App. Environ. Microbiol.* **59**, 101–108.

Van Cappellen P. and Wang Y. (1996) Cycling of iron and manganese in surface sediments: a general theory for the coupled transport and reaction of carbon, oxygen, nitrogen, sulfur, iron, and manganese. *Am. J. Sci.* **296**, 197–243.

Werne J. P., Hollander D. J., Behrens A., Schaeffer P., Albrecht P. and Sinninghe Damsté J. S. (2000) Timing of early diagenetic sulfurization of organic matter: a precursor-product relationship in Holocene sediments of the anoxic Cariaco Basin, Venezuela. *Geochim. Cosmochim. Acta* **64**, 1741–1751.

Werne J. P., Lyons T. W., Hollander D. J., Formolo M. J. and Sinninghe Damsté J. S. (2003) Reduced sulfur in euxinic sediments of the Cariaco Basin: sulfur isotope constraints on organic sulfur formation. *Chem. Geol.* **195**, 159–179.

Werne J. P., Hollander D. J., Lyons T. W. and Sinninghe Damste J. S. (2004) Organic sulfur biogeochemistry: Recent advances and future directions. In *Sulfur Biogeochemistry – Past and Present* (eds. J. P. Amend, K. J. Edwards and T. W. Lyons). Geological Society of America, pp. 135–150.

Westrich J. T. and Berner R. A. (1984) The role of sedimentary organic matter in bacterial sulfate reduction: the G-model tested. *Limnol. Oceanogr.* **29**, 236–249.

Wijsman J. W. M., Middelburg J. J., Herman P. M. J., Böttcher M. E. and Heip C. H. R. (2001) Sulfur and iron speciation in surface sediments along the northwestern margin of the Black Sea. *Mar. Chem.* **74**, 261–278.

Wilkin R. T. and Barnes H. L. (1996) Pyrite formation by reactions of iron monosulfides with dissolved inorganic and organic sulfur species. *Geochim. Cosmochim. Acta* **60**, 4167–4179.

Wortmann U. G., Bernasconi S. M. and Böttcher M. E. (2001) Hypersulfidic deep biosphere indicates extreme sulfur isotope fractionation during single-step microbial sulfate reduction. *Geology* **29**, 647–650.

Zopfi J., Kjær T., Nielsen L. P. and Jørgensen B. B. (2001) Ecology of Thioploca spp nitrate and sulfur storage in relation to chemical microgradients and influence of Thioploca spp.: on the sedimentary nitrogen cycle. *App. Environ. Microbiol.* **67**, 5530–5537.

Zopfi J., Böttcher M. E. and Jørgensen B. B. (2008) Biogeochemistry of sulfur and iron in Thioploca-colonized surface sediments in the upwelling area off central Chile. *Geochim. Cosmochim. Acta* **72**, 827–843.

Associate editor: Robert C. Aller